




Publication Year	2021
Acceptance in OA @INAF	2022-03-11T14:48:39Z
Title	s-processing in AGB Stars Revisited. III. Neutron Captures from MHD Mixing at Different Metallicities and Observational Constraints
Authors	Busso, Maurizio; VESCOVI, DIEGO; Palmerini, Sara; CRISTALLO, Sergio; Antonuccio-Delogu, Vincenzo
DOI	10.3847/1538-4357/abca8e
Handle	http://hdl.handle.net/20.500.12386/31549
Journal	THE ASTROPHYSICAL JOURNAL
Number	908



***s*-processing in AGB Stars Revisited. III. Neutron Captures from MHD Mixing at Different Metallicities and Observational Constraints**

Maurizio Busso^{1,2} , Diego Vescovi^{3,2,4} , Sara Palmerini^{1,2} , Sergio Cristallo^{4,2} , and Vincenzo Antonuccio-Delogu⁵ 

¹Department of Physics and Geology, University of Perugia, Via A. Pascoli snc, I-06123 Perugia, Italy; maurizio.busso@unipg.it, maurizio.busso@pg.infn.it

²INFN, section of Perugia, Via A. Pascoli snc, I-06123 Perugia, Italy

³Gran Sasso Science Institute, Viale Francesco Crispi, 7, I-67100 L'Aquila, Italy

⁴INAF, Observatory of Abruzzo, Via Mentore Maggini snc, I-64100 Collurania, Teramo, Italy

⁵INAF, Catania Astrophysical Observatory, Via S.Sofia 79, I-95123 Catania, Italy

Received 2020 September 2; revised 2020 November 11; accepted 2020 November 14; published 2021 February 11

Abstract

We present post-process neutron-capture computations for Asymptotic Giant Branch (AGB) stars of $1.5\text{--}3 M_{\odot}$ and metallicities $-1.3 \leq [\text{Fe}/\text{H}] \leq 0.1$. The reference stellar models are computed with the FRANEC code, using the Schwarzschild's criterion for convection; our motivations for this choice are outlined. We assume that MHD processes induce the penetration of protons below the convective boundary, when the Third Dredge Up occurs. There, the ^{13}C *n*-source can subsequently operate, merging its effects with those of the $^{22}\text{Ne}(\alpha, n)^{25}\text{Mg}$ reaction, activated at the temperature peaks characterizing AGB stages. This work has three main scopes. (i) We provide a grid of abundance yields, as produced through our MHD mixing scheme, which are uniformly sampled in mass and metallicity. From this, we deduce that the solar *s*-process distribution, as well as the abundances in recent stellar populations, can be accounted for, without the need of the extra primary-like contributions suggested in the past. (ii) We formulate analytic expressions for the mass of the ^{13}C -pockets generated to allow easy verification of our findings. (iii) We compare our results with observations of evolved stars and with isotopic ratios in presolar SiC grains, also noticing how some flux tubes should survive turbulent disruption, carrying C-rich materials into the winds even when the envelope is O-rich. This wind phase is approximated through the *G*-component of AGB *s*-processing. We conclude that MHD-induced mixing is adequate to drive slow *n*-capture phenomena accounting for observations; our prescriptions should permit its inclusion into current stellar evolutionary codes.

Unified Astronomy Thesaurus concepts: [Asymptotic giant branch stars \(2100\)](#); [S-process \(1419\)](#); [Stellar nucleosynthesis \(1616\)](#); [Meteorite composition \(1037\)](#); [Magnetohydrodynamics \(1964\)](#); [Barium stars \(135\)](#)

1. Introduction: Setting the Stage

Stars are made of plasmas, in which physical conditions range over several orders of magnitude in pressure, temperature and density. In them, many hydro-dynamical and magneto-hydro-dynamical processes occur in variable and complex ways, which are characterized by micro- and macro-turbulence phenomena with Reynolds' numbers that are well beyond the limits experimentally studied in terrestrial laboratories (Tsuji 2009) and actually also beyond our capability of detailed, quantitative modeling. Evolutionary computations can only ascertain that traditional one-dimension models are largely insufficient to account for short- and long-term processes of stirring and mixing (Stancliffe & Lattanzio 2011), and often limit themselves to simulate schematically the layers affected by pure convection, using the mixing length theory or some other simplified approaches (see Salaris 2007; Salaris & Cassisi 2015, and references therein). They can also address in similar ways the regions of semi-convection, distinguishing between the two mixing schemes through the Schwarzschild's and Ledoux's criteria for stability, both of which are based on simple polytropic approaches (Chandrasekhar 1939). In modern computations, they may include also some (but not all) of the effects induced by rotation (see e.g., Heger et al. 2000; Huang 2004; Ekström et al. 2012; Piersanti et al. 2013; Matrozis & Stancliffe 2017, and references therein). These limits in existing efforts are unavoidable and they make it clear that the real behavior of stellar plasmas is more complex than our basic descriptions. Even for the Sun, a large family of different dynamical processes induce variations in the structure, hence in the irradiance, over timescales ranging from minutes to billions of years (Kopp 2016).

It is therefore expected that also in the advanced stages of their life, during and after the ascent to the Red Giant Branch (RGB), stars sharing the same evolutionary scheme of the Sun experience mass and momentum transfer at different speeds (Boothroyd et al. 1995; Charbonnel & Balachandran 2000). These are the stellar objects of low and intermediate mass (LMS and IMS: i.e., those in the mass ranges $1\text{--}3 M_{\odot}$ and 3 to about $8 M_{\odot}$, respectively). The exercise of imagining, for them, which circulation or diffusion mechanisms might be at play is required at least by the need of reproducing isotopic and elemental observations that cannot be explained by usual models with pure convection (Busso et al. 1999, 2010; Nollett et al. 2003; Karakas & Lattanzio 2014). Recent research has focused on many such mechanisms, from relatively fast dynamical (Denissenkov & Tout 2003; Battino et al. 2016, 2019; Pignatari et al. 2016) and magneto-hydro-dynamical (Busso et al. 2007; Nordhaus et al. 2008) processes with speeds up to several m/sec, all the way down to various forms of slow (less than 1 cm/sec) diffusive mixing (Eggleton et al. 2006, 2008; Charbonnel & Zahn 2008; Stancliffe 2015).

It is now ascertained that some abundance observations provide constraints at least on the velocity, and possibly on the nature, of the dynamical mixing phenomena occurring (Herwig et al. 2003; Busso et al. 2007; Denissenkov & Merryfield 2011; Palmerini et al. 2011; Liu et al. 2015). This is so in particular for Li (Charbonnel & Lagarde 2010; Palmerini et al. 2011) and for the enrichment in neutron-rich elements (Cristallo et al. 2009, 2011, 2015b; Trippella et al. 2016) occurring in the final evolutionary stages, approaching the RGB asymptotically (AGB phases). Indeed, it has been known for more than 30 yr now that

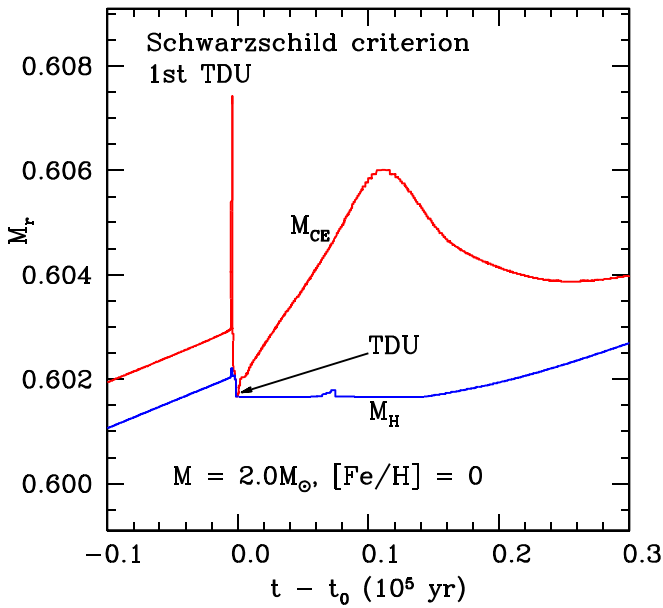


Figure 1. The first occurrence of the envelope penetration in a Third Dredge Up episode, computed with the FRANEC code for a $2 M_{\odot}$ star of solar composition. The figure shows in red the innermost border of the convective envelope (M_{CE}) and in blue the position of the H/He interface (M_H), with its characteristic minimum (*post-flash dip*) before H-burning restarts. The parameter t_0 is the stellar age at the moment of the TDU episode shown. Note how, of the rather long duration of the post-flash dip ($\sim 10^4$ yr), only a very short fraction is occupied by TDU (~ 100 yr).

the bulk of neutron fluxes for the required nucleosynthesis episodes is produced in ^{13}C reservoirs (Gallino et al. 1988, 1998; Arlandini et al. 1999; Käppeler et al. 2011), formed at the recurrent penetration of envelope convection into the He-rich buffer of the star, which is called the Third Dredge Up (TDU). This last phenomenon has now been observed to occur over the whole range of the masses here considered and down to about $1 M_{\odot}$ stars (Shetye et al. 2019). The mentioned suggestions on *s*-processing have been verified in some detail directly on the observations of carbon stars (Abia et al. 2001, 2002, 2003). Formation of the ^{13}C reservoir follows the retreat of shell convective instabilities developing in the He-layers (Straniero et al. 1995; Herwig 2005) and requires that an important fraction of the He-rich buffer (hereafter *He-intershell zone*) be swept by the penetration of protons from the envelope (Trippella et al. 2014, hereafter Paper I), within the time interval over which the bottom border of envelope convection reaches its maximum downward expansion (see Figure 1, for a star of solar metallicity⁶).

The limited duration in time of the TDU phenomenon ($\simeq 100$ yr) plays in favor of rather fast mixing mechanisms (of the order of a few m s^{-1}). This can for example be achieved in the case of the unimpeded buoyancy of magnetic flux tubes, which may occur given the specific polytropic structure of high index ($n \geq 3$) and the fast density decline ($\rho \propto r^k$, with $k \ll -1$), prevailing in the radiative layers below the convective envelope, which provide an exact analytical solution to MHD equations in the form of free, accelerating expansion (Nucci & Busso 2014). We notice how the alternative to look for exact solutions in a simplified geometry would be that of performing detailed 3D

numerical simulations. This approach has indeed seen important attempts (see e.g., Stancliffe et al. 2011, and references therein), but is much more difficult to implement in general.

The first neutron-capture nucleosynthesis computations presented in the MHD scenario (Trippella et al. 2016) demonstrated that the peculiar profile of ^{13}C in the reservoirs thus formed was suitable for reproducing detailed isotopic patterns in presolar grains that could not be fitted otherwise, which is in agreement with previous indications by Liu et al. (2015). This was shown to be possible in a framework that could also mimic the solar *s*-process distribution; it was also suggested how extrapolations of that model could satisfy other observational requirements. In this contribution we want to extend the work presented in Trippella et al. (2016, hereafter Paper II) by computing the formation of MHD-induced ^{13}C pockets over a wide range of metallicities and for FRANEC evolutionary models of 1.5 – $3 M_{\odot}$. In so doing, we also provide analytic fits to the extension of the ^{13}C -pockets to make our results easily reproduced by others. In Section 2, we outline our approach and assumptions, as well as the mentioned analytic fits, together with general results as a function of mass and metallicity. Subsequently, in Section 3 we discuss how our results can be used, once weighted in mass and time using a common choice for the Initial Mass Function (IMF) and a Star Formation Rate (SFR) taken from the literature, in accounting for the abundances gradually built by Galactic evolution and now observed in stars of the Galactic disk, from our solar system to the most recent stellar populations of young open clusters. This is a synthetic anticipation from a more extended work of chemo-dynamical Galactic evolution that we are pursuing. Finally, in Section 4 we compare the abundance distributions produced by our models at the surface of evolved stars with some of the observational constraints available either from actual AGB and post-AGB stars of various families, or from the isotopic analysis of trace elements in presolar grains. The series of comparisons presented in this paper have the final goal of guaranteeing that our predictions can be safely and robustly verified. As a consequence of these checks, our mixing prescriptions have now been delivered for direct inclusion into full stellar models of the FUNS series (Cristallo et al. 2018): preliminary results of such an inclusion were presented in a recently published paper (Vescovi et al. 2020).

2. Modeling the TP-AGB Evolution and its Nucleosynthesis

2.1. The Stellar Models and the Proton Mixing

In Paper II we implemented the exact solution of MHD equations, as found by Nucci & Busso (2014), in the form of free buoyancy for magnetic flux tubes. On that basis, we computed neutron-capture nucleosynthesis in a star of $1.5 M_{\odot}$ of a metallicity slightly lower than solar. We then adopted the ensuing model as a proxy for stars in the mass range from 1 to $3 M_{\odot}$, at Galactic-disk metallicities. This preliminary, simplified extrapolation was motivated by previous suggestions advanced in Maiorca et al. (2011, 2012) and in Paper I. In these works, starting from parameterized extensions of the ^{13}C pocket, it had actually been found that the nuclear yields of a star characterized by parameters (mass, initial metallicity, extension of the ^{13}C reservoir) very similar to those of the model shown in Paper II would provide a reasonable approximation to the average yields in the Galactic disk, thus mimicking the enrichment of the solar system and of recent stellar populations in neutron-rich nuclei.

⁶ We remind the reader that the heavy-element content of a star relative to the Sun, i.e., its *metallicity*, is commonly indicated in logarithmic notations, with the parameter $[\text{Fe}/\text{H}] = \text{Log}(X(\text{Fe})/X(\text{H}))_{\text{star}} - \text{Log}(X(\text{Fe})/X(\text{H}))_{\odot}$.

We now want to complete this job by estimating, for a wide metallicity range ($-1.3 \leq [\text{Fe}/\text{H}] \leq 0.1$) and for three reference stellar masses (1.5, 2.0 and $3.0 M_{\odot}$, computed ad-hoc with the FRANEC evolutionary code), the extensions of the ^{13}C pockets formed in the hypotheses of Paper II. In particular, we assumed that proton penetration from the envelope into the He-rich layers at every TDU episode occurs as a consequence of the activation of a stellar dynamo, with the ensuing buoyancy into the envelope of highly magnetized structures. These structures push down poorly magnetized material, forcing it into the radiative He-rich layers.

As mentioned previously, the stellar models were computed with the FRANEC evolutionary code, which uses the Schwarzschild's criterion for convection; for a description of the physical assumptions characterizing the code, see for example Straniero et al. (2003).

It is today generally recognized that some form of extension of the convective border with respect to a pure Schwarzschild's limit is needed (Freytag 1996); for more detail, see the discussion on this point by Ventura et al. (2020) and the references cited therein. However, given that we aim to look at how the ^{13}C n -source is formed in MHD-driven mechanisms, our approach must be that of attributing any extension of such a border to magnetic effects, without the admixture of different schemes, each based on its own free parameters, which would make the disentangling of different effects ambiguous. Only after this work is completed will we be authorized to check for possible changes induced by a different treatment of the convective extension, as is in fact done in Vescovi et al. (2020). Originally, our models adopted a Reimers' criterion for mass loss, with the parameter η set to 1.0 for 1.5 and $2.0 M_{\odot}$ models, and to 3 for $3.0 M_{\odot}$ models. In making post-process computations for nucleosynthesis, we instead adopted the more efficient mass loss rates of the FRUITY repository. The rate of mass loss through stellar winds remains largely unknown, which introduces important uncertainties on the composition of the stellar envelopes (Stancliffe & Jeffery 2007).

In this context, it will be necessary to compute not only the average abundances gradually formed in the envelopes but also those of the He-shell material cumulatively transported by TDU episodes. This represents an s -process-enhanced, C-rich phase that is averaged over the efficiency of mixing, which has for several years been called the G component (Zinner 1998). In our models, the G -component carries abundances that are very similar to those of flux tubes that, due to strong magnetic tension, survive destruction by turbulence in the convective envelope and later open in the wind; as occurs in the Sun (Pinto et al. 2016). There is actually some support in the current literature for the existence of such magnetized wind structures in evolved stars (Rosner et al. 1991; Rosner 1992; Soker & Kastner 2003; Sabin et al. 2015). These blobs would maintain an unmixed C- and s -process rich composition, which is typical of the He-intershell zone, even when the rest of the envelope is O-rich. In our models, it is feasible to use the G -component to approximate the abundances of this wind phase because of the high neutron fluences generated in each pulse-interpulse cycle, which usually allow the effects of the most recent nucleosynthesis episode to dominate over the previous ones. The relevance of this approximation will become clear in considering the isotopic admixtures of presolar SiC grains enriched in s -process elements (see Section 4.1).

2.2. The ^{13}C Pocket and the Ensuing Nucleosynthesis

In the above approach, the extension and profile of any proton reservoir formed are computed according to the formulation of

Paper II (see its equations from 14 to 17), after verifying that the required conditions, stated in Nucci & Busso (2014), are satisfied. The occurrence of the proper physical conditions was ascertained as follows.

(i) The MHD solution found in Nucci & Busso (2014) and expressed in Equation (5) of Paper II ($\rho(r) \propto r^k$, with $k < -1$) was verified on the model structures computed with the stellar code, for every TDU occurrence (in the He-rich layers k turns out to be always lower than -3). Since the condition on k derives from an exact solution, we expect that the regression coefficients be close to 1. They are always larger than 0.98 over about half of the intershell region (in mass). In the layers of that zone where protons penetrate according to the equations of Paper II they are even larger, reaching typical values as indicated here in Figure 1.

(ii) Over the layers thus selected, we computed the kinematic viscosity η from the approach by Schekochihin et al. (2004), as:

$$\eta(r) \propto \frac{v_{\text{th}}(r)}{n(r)\sigma(r)} \quad (1)$$

where $v_{\text{th}}(r)$ is the local thermal velocity and $\sigma(r)$ is the ionic cross section, $\pi l(r)^2$, l being proportional to the DeBroglie's wavelength, $l \propto h/(mv_{\text{th}})$. From this, we estimated the dynamical viscosity:

$$\mu(r) = \eta(r)\rho(r). \quad (2)$$

We then assumed from Spitzer (1962) and Schekochihin et al. (2004) the value of the magnetic Prandtl number, as:

$$P_m(r) = \frac{\eta}{\nu} \simeq 10^{-5} \frac{T(r)^4}{n(r)} \quad (3)$$

(where ν is the magnetic viscosity) and verified that values of P_m were always much larger than unity (they turned out to be always larger than 10 over the selected layers). (iii) We also requested that the third condition posed by Nucci & Busso (2014) were verified, namely that the region of interest had a low value for the dynamical viscosity (as defined in Equation (2)), i.e., values of μ much smaller than in more internal regions. This condition was again found to hold easily, due to the steep growth of the density in the innermost layers of the He-intershell zone. A few examples of the fits obtained under the above conditions, with the resulting masses for the proton reservoirs are shown in Figure 2.

As mentioned, the proton distribution resulting in the above layers can be computed by the equations presented in Paper II. The extensions in mass M_p of the reservoirs vary in roughly quadratic (parabolic) ways as a function of the core mass m_{H} (which specifies the moment in the AGB evolution when a given TDU episode occurs). Regression coefficients are in this case between 0.97 and 0.99.

Indicating by f the relative metallicity in a linear scale ($f = \text{Fe}/\text{Fe}_{\odot} = 10^{[\text{Fe}/\text{H}]}$), we can then write:

$$M_p = a(f) \cdot m_{\text{H}}^2 + b(f) \cdot m_{\text{H}} + c(f) \quad (4)$$

where the three coefficients $a(f)$, $b(f)$, $c(f)$ are presented in Table 1. We fitted the dependence of the coefficients on f through further quadratic forms only for the sake of illustration, albeit there is no physics in this procedure, just an analytic formulation given for convenience. The dependence on the two parameters m_{H} and $f = \text{Fe}/\text{Fe}_{\odot}$, is then shown in Figure 3 for

Table 1
The Coefficients of the Parabolic Dependence of M_p vs. m_H for Three Different Metallicities and Three Different Stellar Masses

[Fe/H]	Coefficients of M_p in Equation (4)								
	$M = 1.5 M_\odot$			$M = 2.0 M_\odot$			$M = 3.0 M_\odot$		
	a	b	c	a	b	c	a	b	c
-0.50	-1.3300	1.7040	-0.5414	-0.5070	0.6680	-0.2164	0.019	0.0426	-0.0366
-0.30	-2.0050	2.4775	-0.7594	0.9646	-1.2658	0.4180	-0.8647	1.0337	-0.3042
0.00	-6.6146	8.3383	-2.6217	-1.3566	1.7393	-0.5527	-0.1373	0.1396	-0.0298

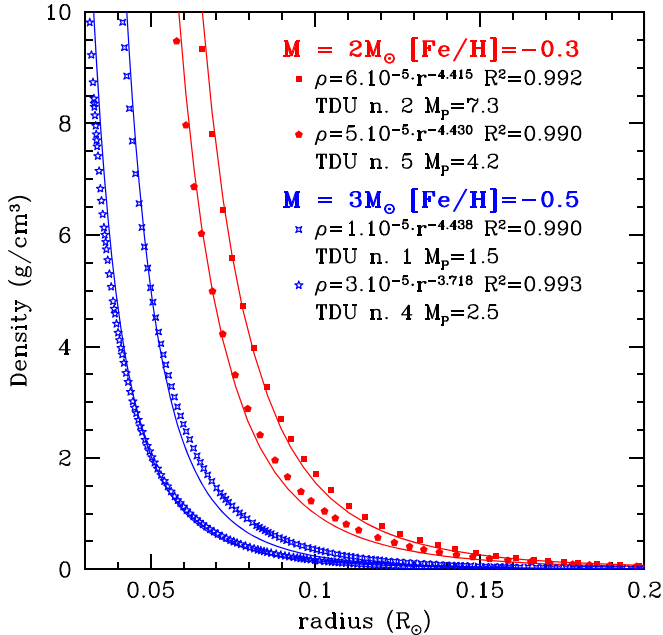


Figure 2. Examples of how the density distributions below the formal convective envelope bottom (defined by the Schwarzschild’s criterion) agree with the requirement of being exact power laws of the radius with large ($k < -3$) negative exponents. The cases shown are from the second and fifth TDU occurrence in a $2 M_\odot$ star of half-solar metallicity and from the first and fourth TDU occurrence in a $3 M_\odot$ star of one-third-solar metallicity. The fitting power laws are shown, with their regression coefficients. Also indicated are the resulting masses M_p of the proton reservoirs, expressed in units of $10^{-3} M_\odot$. In models for the largest stellar masses considered ($3 M_\odot$) the validity of the solution is generally limited to layers considerably thinner than for lower mass models.

the reference stellar models, over a range of metallicities typical of the Galactic disk

Once the extension of the ^{13}C reservoirs and the profile in them of the ^{13}C abundance were estimated for every TDU episode of the mentioned stellar models, we used the NEWTON post-process code (see Paper II) for computing the nucleosynthesis induced by the combined activation of the neutron sources $^{13}\text{C}(\alpha, n)^{16}\text{O}$ and $^{22}\text{Ne}(\alpha, n)^{25}\text{Mg}$.

As in previous issues of this series of works, the post-process code carefully imports from the stellar model the relevant physical parameters (extension of the intermediate convective layers at TPs, their temperature and density profiles in mass and time, the timing and extension of dredge-up phenomena, the mass of the envelope, gradually eroded by the growth of the core mass m_H and by mass loss, etc.). Reference solar abundances were taken from Lodders & Palme (2009). The cross section database is from the on-line compilation KADONIS, v0.3 (Dillmann et al. 2006), with integrations from the upgrade KADONIS v1.0 (Dillmann et al. 2014). These extensions require some careful considerations,

in particular for the stellar enhancement factors (SEFs). Indeed, in KADONIS v1.0, these corrections are accompanied with the alternative suggestions proposed by Rauscher (2012), called X -factors. These last are sometimes sharply different from the traditional SEFs used by many groups and also by us so far. The choice of which stellar corrections to apply requires therefore some iterative checks, to be performed on preliminary computations (see later and Figure 4). Recent results from the n_TOF collaboration (Massimi et al. 2019; Mazzone et al. 2020) are also included. Concerning weak interactions, their rates are normally taken from Takahashi & Yokoi (1987), Takahashi et al. (1987). For the cases in which bound-state decays are known to occur in ionized plasmas, the corrections discussed in Takahashi & Yokoi (1983) and in Table 5 of Takahashi & Yokoi (1987) were applied, although these are probably still insufficient to mimic real stellar conditions.

On this point, we must remember that weak interaction rates in stars remain the largest source of uncertainty in s -processing. This is, for example, evident in the important case of the s -only nucleus ^{187}Os (produced by decay of its parent ^{187}Re , which in laboratory is a very long-lived isotope, with $t_{1/2}^{\text{lab}} \simeq 40$ Gyr). The parent is known to undergo a bound-state decay in stellar conditions: due to this fact, when it is completely ionized, it decays in a few tens of years (Litvinov et al. 2011). The problem is that s -process conditions should correspond to partial ionization, and one would need to interpolate over nine orders of magnitude. We adopted here the Local Thermodynamic Equilibrium approach by Takahashi & Yokoi (1987) for the dependency of the ^{187}Re rate on temperature and density, but the treatment is largely insufficient. Moreover, it is unknown what kind of change is induced on the ^{187}Re half-life by the process of astration, due to which the nucleus enters successive stellar generations, where it is taken at high temperature, so that its decay rate certainly increases; however, we do not know by how much. Consequently, in our models ^{187}Os is only partly produced (see Figure 4(b) and later Figure 14). We are forced, in this respect, to accept that the quantitative reproduction of its abundance must wait for new measurements in conditions simulating the stellar ones.

Similar uncertainties exist for several nuclei immediately following reaction branchings in the s -process path, where weak interaction rates dominate the production. A remarkable example is that of the couple ^{176}Lu - ^{176}Hf (see Figure 15). The first nucleus is a long-lived isotope in laboratory conditions (with a half-life of 36 Gyr, see Söderlund et al. 2004). In stars, it presents a short-lived isomeric state. A direct link of this with the ground state via dipole transitions is forbidden at the temperature where ^{13}C burns (0.9×10^8 K), so that the two states of ^{176}Lu effectively behave as separate nuclei. However, when a thermal instability develops in the AGB environment, the locally high temperature ($T \geq 3 \times 10^8$) can excite a number of overlying mediating states and the isomeric level gets thermalized. These complications, which were studied in

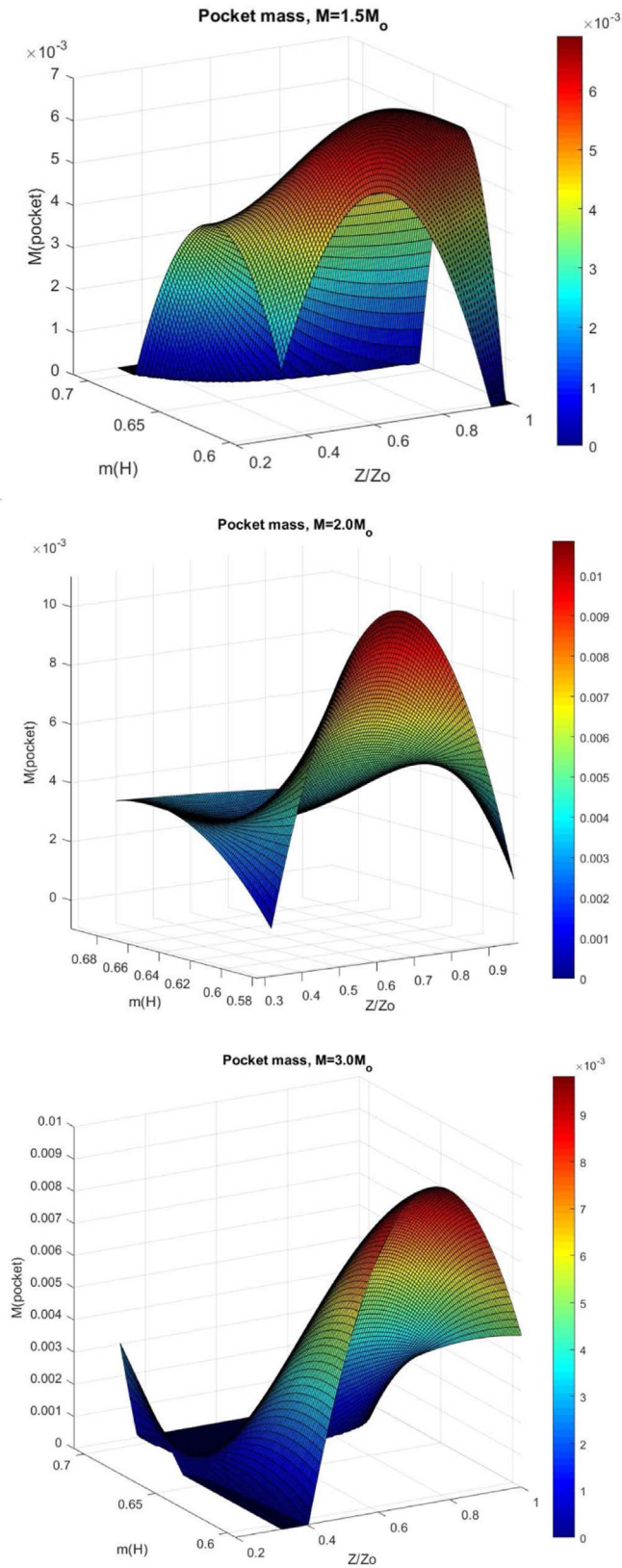


Figure 3. A synthetic view of the dependence of the pocket mass M_p on the core mass (m_{H}) and the relative metallicity ($f = X(\text{Fe})/X(\text{Fe})_{\odot}$) for the reference models, at typical Galactic disk metallicities. The plots are pure fits to model results and cannot be extrapolated beyond their limits. Note that the apparent *spike* at the low left end in the bottom panel is real: in the FRANEC code, at low metallicity, a $3.0 M_{\odot}$ model star behaves almost as an IMS, with TDU (hence also ^{13}C pockets) starting at relatively high values of the core mass.

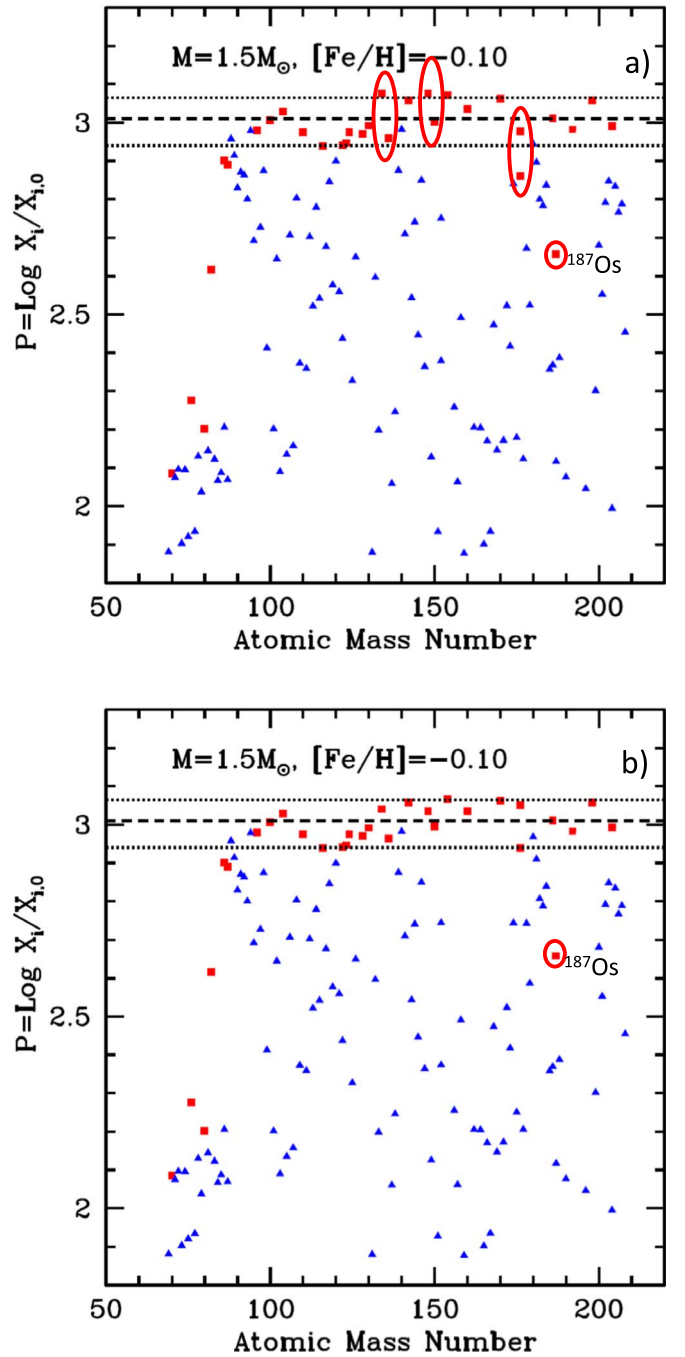


Figure 4. The production factors of nuclei beyond Fe in the He-intershell layers for the model of a $1.5 M_{\odot}$ star of metallicity slightly lower than solar, mimicking rather well the solar distribution of s -only nuclei (red squared dots). The average overabundance for s -only nuclei is slightly higher than 1000 (dashed line: a general fiducial uncertainty of 15% is indicated through the dotted lines). The other symbols (in blue) represent nuclei only partly contributed by s -processing. Panel (a) shows the discrepancies found on close-by s -only nuclei in the preliminary computations made with the nuclear parameters mentioned in the text. The alternative choices we suggest permit to reduce the scatter considerably, as shown in panel (b).

detail by Klay et al. (1991a, 1991b), Käppeler et al. (2006), sum to the fact that the half-life above about 20–22 keV becomes very short and dependent on temperature, so that ^{176}Lu actually behaves as a thermometer (Klay et al. 1991a). In our results, ^{176}Lu and its daughter ^{176}Hf are formally inside a *reasonable* general error bar of $\simeq 15\%$ (see Figures 4 and 14),

laying, however, at its extremes. Any further improvement must wait for better nuclear inputs. Another important case of weak interaction effects concerns ^{134}Cs , whose β^- decay to ^{134}Ba is crucial in fixing the abundance ratio of the two s -only isotopes ^{134}Ba and ^{136}Ba . The value taken from Takahashi & Yokoi (1987) and its temperature dependence is very uncertain (see discussion in Kaeppler et al. 1990). Again, we must be content that, despite this, the model abundances of ^{134}Ba and ^{136}Ba lie within the general fiducial error bar. Improving on this would require dedicated experimental data. Some of the relevant radioactive nuclei along the s -path that are suitable to be affected by these specific uncertainties are now in the program of the new experiment PANDORA (Mascali et al. 2020), which in 2022 will start measuring decay rates in ionization conditions that are as similar as possible to the stellar ones.

As already suggested in Paper II, s -processing in the Galaxy has the remarkable property that one can identify a specific model (characterized by a low initial mass and a metallicity typical of the Galactic disk within 2–3 Gyr before the Sun is formed), which roughly simulates the solar distribution. Figure 4 shows one such case, where indeed the abundances of s -only nuclei (indicated by heavy squared dots) have similar production factors, roughly averaging at about 1000. This model grossly represents a sort of average of what can be more properly obtained by the chemical evolution of the Galaxy, but this last is of course needed to account for the different effects of stellar temperatures in differently massive stars. However, the *average* model is a suitable preliminary calculation to be performed, on which we can tentatively test the uncertain corrections to the cross sections mentioned previously.

The top panel of Figure 4 (panel (a)) shows the results computed using the corrective X – *factors* to the cross sections from Rauscher (2012). It is evident that although the distribution for s -only nuclei (red dots) is rather flat (as it should be for producing them in solar proportions), there exist cases in which adjacent s -only nuclei show considerably discrepant abundances (see the red evidencing marks). If one normalizes the average to 1.0, then these discrepancies become particularly evident for ^{134}Ba (1.21) and ^{136}Ba (0.89); then for ^{148}Sm (1.20) and ^{150}Sm (1.01) and for ^{176}Lu (0.95) and ^{176}Hf (0.73). These are all complex cases, which are also affected by large uncertainties on β^- -decay rates (for ^{134}Cs , ^{149}Sm , $^{176}\text{Lu}^g$ and its isomer $^{176}\text{Lu}^m$). However, for all of the nuclei that we have considered, a significant worsening of the distribution is induced by the application of the mentioned X – *factors*, which sometimes imply corrections opposite to the traditional SEFs. Although the uncertainties do not allow us to reject the X – *factor* corrections in general, we made an alternative computation by changing them with the usual SEFs to verify which dataset was more suitable for obtaining a solar-like distribution. The result of this test is presented in Figure 4, panel (b), where it is shown that some improvements are immediately obtained for the three couples indicated previously. The new ratios found in the *average* model are: 1.09 (^{134}Ba), 0.92 (^{136}Ba), 1.08 (^{148}Sm), 0.99 (^{150}Sm), 1.11 (^{176}Lu), 0.88 (^{176}Hf). On this basis, in the rest of this paper we decided to adopt the common SEFs to cross sections, postponing a more detailed check of the corrections by Rauscher (2012) to a separate work.

With the choices thus made, examples of abundance distributions in the envelopes at the end of the TP-AGB stage are shown in Figures 5–7 for various stellar masses and

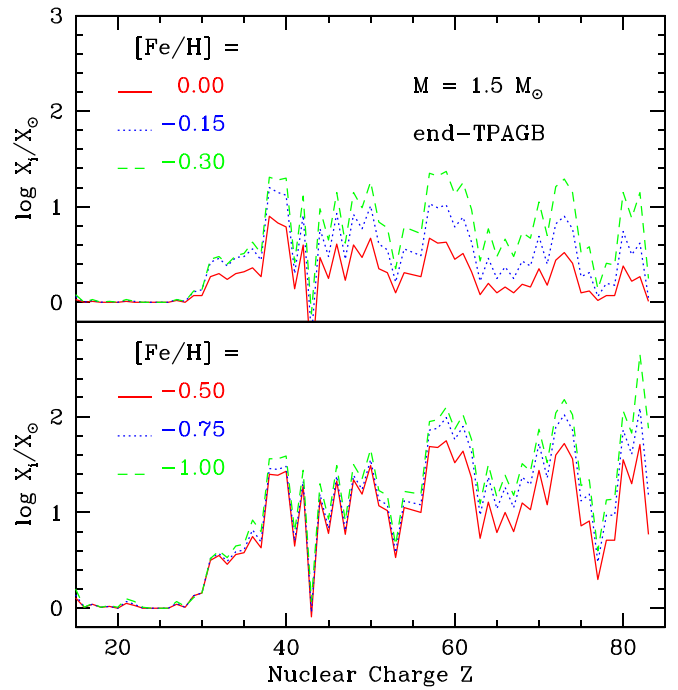


Figure 5. Abundances in the envelope at the last TDU episode computed for stars of initial mass $M = 1.5 M_{\odot}$ at the indicated metallicities.

metallicities. The number of TDU episodes found in the cases shown by the figures is reported in Table 2.

The distributions presented in Figures 5–7 illustrate the increase in the abundances of n -capture elements expected for metal-poor AGB stars, this trend had been previously inferred from parametric models (see e.g., Gallino et al. 1998) and in general permits us to account for the observations of s -elements in AGB stars at different metallicities. This now appears to remain true in computations where the ^{13}C pocket is generated by a physical model not explicitly related to metallicity. This is so because the complex dependence of the pocket masses on the stellar parameters shown in Figure 3 is not sufficient to erase the signatures impressed in the s -process distribution by the fact that, for a *primary-like* neutron source, the neutron exposure grows for decreasing abundances of the seeds (mainly Fe) by which the neutrons are captured.

Since the suggestions by Luck & Bond (1981, 1991), it is common to synthetically represent the s -process distribution in stars with the two indices $[ls/Fe]$ and $[hs/Fe]$, where ls stands for *light s-elements* and hs stands for *heavy s-elements*. They are built with the logarithmic abundances at the first and second s -process peak, near the neutron magic numbers $N = 50$ and $N = 82$. In particular, we follow the suggestions by Luck & Bond (1991) in assuming $[hs/Fe] = 0.25 \cdot ([Ba/Fe] + [La/Fe] + [Nd/Fe] + [Sm/Fe])$, and by Busso et al. (2001) in assuming $[ls/Fe] = 0.5 \cdot ([Y/Fe] + [Zr/Fe])$. Their difference, $[hs/ls] = [hs/Fe] - [ls/Fe]$, is an effective indicator of the neutron exposure, with low neutron fluences feeding primarily the $[ls]$ abundances and high fluences making the $[hs]$ indicator to prevail. In Figures 8–10, the behavior of neutron-capture elements as a function of metallicity in our models is illustrated through the indices thus defined. As clarified many years ago (Gallino et al. 1998), the heaviest s -process isotopes (the so-called *strong* component of the s -process), and in particular ^{208}Pb , grow with metallicity with a trend that is steeper than for the $[hs]$ nuclei, the heaviest isotopes being sited

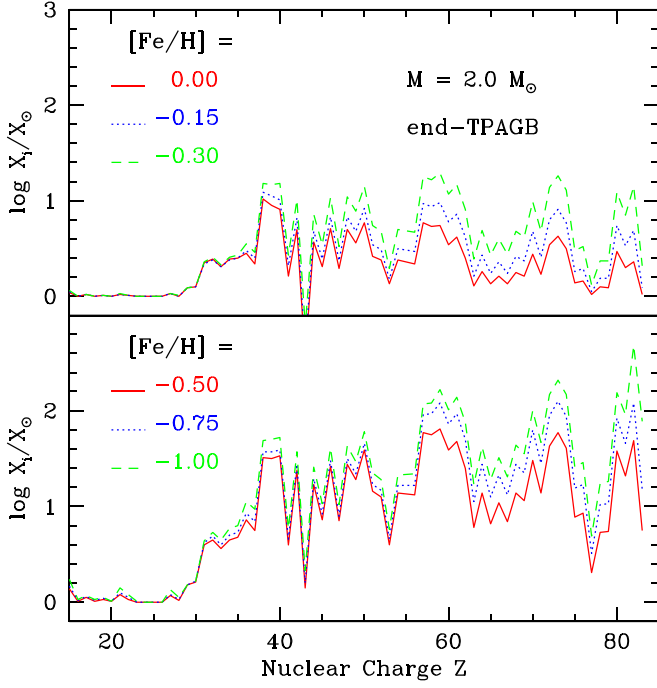


Figure 6. Same as in Figure 5, for models of $2.0 M_{\odot}$.

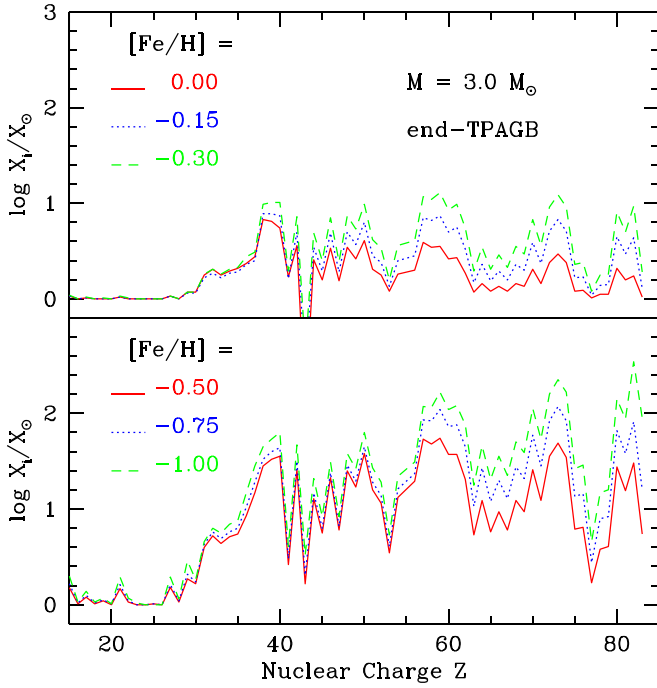


Figure 7. Same as in Figure 5, for models of $3.0 M_{\odot}$.

in correspondence of another magic number of neutrons ($N = 128$). This property is preserved in the present scenario. Figure 11 shows the further increase at low metallicity of lead with respect to the $[hs]$ nuclei, these last representing the $N = 82$ neutron magic number. We notice that the trend of $[Pb/hs]$ shown in the figure is in good agreement with that obtained by a few current models with parametric extra-mixing; for example, those of the STAREVOL and FRUITY collaborations. For more detail on this point, see in particular De Smedt et al. (2014) and Figure 14 in De Smedt et al. (2016).

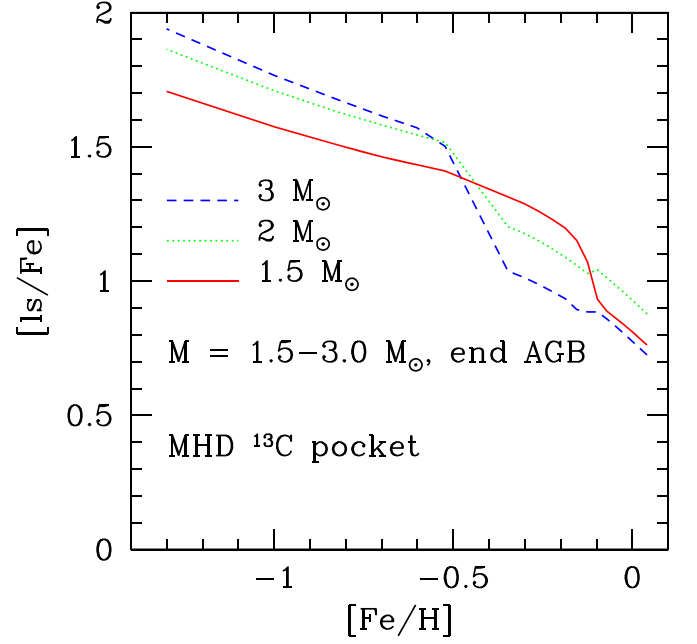


Figure 8. Production factors for elements at the abundance peak near the magic neutron number $N = 50$, as summarized by the $[ls/Fe]$ indicator, for stellar masses $M = 1.5, 2.0$ and $3.0 M_{\odot}$ at various metallicities.

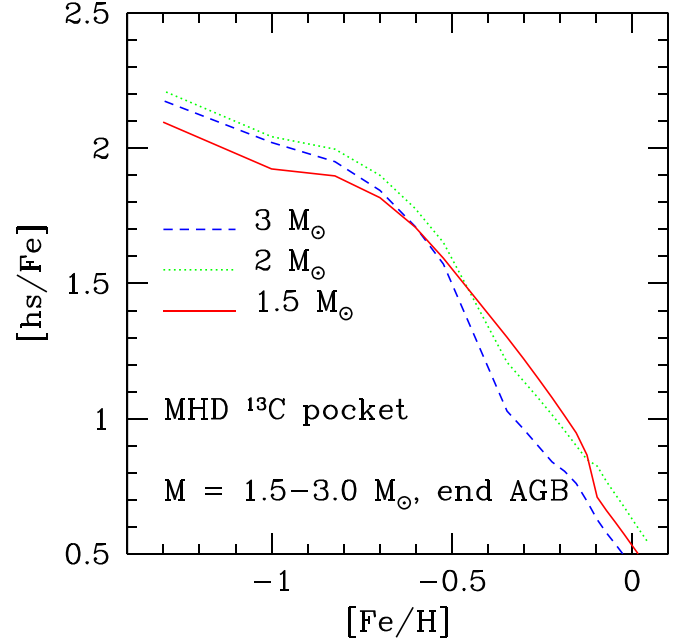


Figure 9. Production factors for elements at the abundance peak near the magic neutron number $N = 82$, as summarized by the $[hs/Fe]$ indicator, for stellar masses $M = 1.5, 2.0$ and $3.0 M_{\odot}$ at various metallicities.

3. Reproducing Constraints from the Sun and Recent Stellar Populations

The effects of an efficiency in s -processing that increases toward lower metallicities are then mediated by the rate at which stars form as a function of the metal content of the Galaxy and of its age, these two parameters are linked by an extremely nonlinear and probably non-unique (Casali et al. 2020) relation. To mimic abundances of the solar neighborhoods, we used an Age–Metallicity relation that was shown to be valid for that region (Maiorca et al. 2011, 2012) to switch

Table 2
General Characteristics of the TDU PHASES where the Conditions for Forming ^{13}C Pockets are Found, According to the Criteria Exposed in the Text

[Fe/H]	Number of TDU Episodes and their Maximum/Minimum Extension in Mass								
	$M = 1.5 M_{\odot}$			$M = 2.0 M_{\odot}$			$M = 3.0 M_{\odot}$		
	N	ΔM_{\min}	ΔM_{Max}	N	ΔM_{\min}	ΔM_{Max}	N	ΔM_{\min}	ΔM_{Max}
-0.50	11	3.6×10^{-4}	1.5×10^{-3}	13	1.5×10^{-3}	3.6×10^{-3}	11	2.4×10^{-4}	3.7×10^{-3}
-0.30	10	7.2×10^{-4}	1.5×10^{-3}	13	2.2×10^{-5}	1.7×10^{-3}	13	1.0×10^{-4}	2.2×10^{-3}
0.00	11	1.5×10^{-4}	7.1×10^{-4}	12	3.8×10^{-4}	1.6×10^{-3}	17	1.0×10^{-4}	2.1×10^{-3}

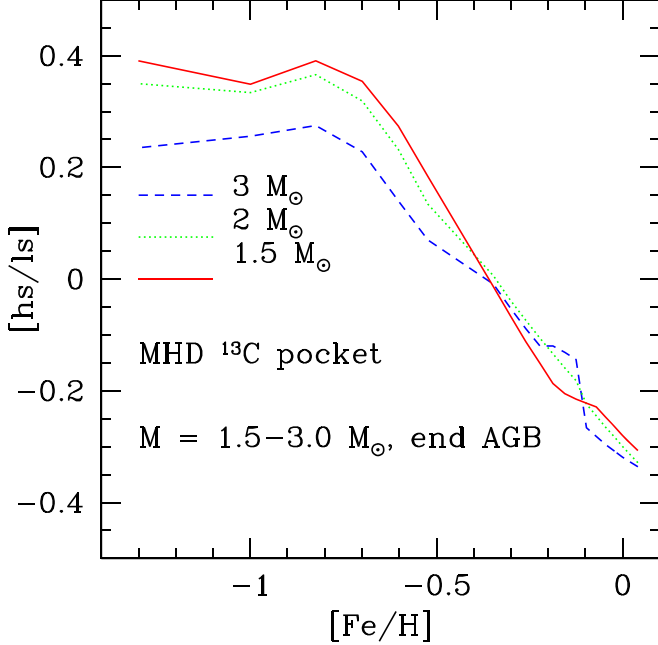


Figure 10. The logarithmic ratios of abundances at the two main s -process peaks for $N = 50$ and $N = 82$, as summarized by the $[\text{hs}/\text{ls}]$ indicator, for the same cases shown in the previous figures.

between the original metal content of a stellar model and the Galactic age to which its formation roughly corresponds. The results are shown in Figures 12 and 13 for the extreme cases of stellar masses $M = 1.5 M_{\odot}$ and $M = 3.0 M_{\odot}$.

As Figure 12 illustrates (see its panel (a)), for low stellar masses the production factors of elements near the two main s -process abundance peaks remain very similar, confined in a small range of less than 0.3 dex, for quite a long period in the Galactic disk before the solar metallicity $[\text{Fe}/\text{H}] = 0$ is reached (a few Gyr). This is not the case for larger masses (see Figure 13), which do, however, have a lower weight in the IMF. As discussed in Maiorca et al. (2012), this condition is essential to permit a growth of s -element abundances that continues after the epoch of the solar formation maintaining a roughly constant $[\text{hs}/\text{ls}]$ ratio, as observed in Young Open Clusters. We are therefore confident that our scenario fulfills this basic constraint of Galactic chemical evolution, which was previously met only by varying parametrically the amount of ^{13}C burnt and its distribution.

We have for the moment simulated such a chemical evolution by weighting the stellar production factors of our models for Galactic disk metallicities. We considered for this the range $-1.0 \lesssim [\text{Fe}/\text{H}] \lesssim 0.0$; i.e., by excluding the most metal-poor and the the most metal-rich (super-solar) models. We adopted a Salpeter IMF and the mentioned history of the

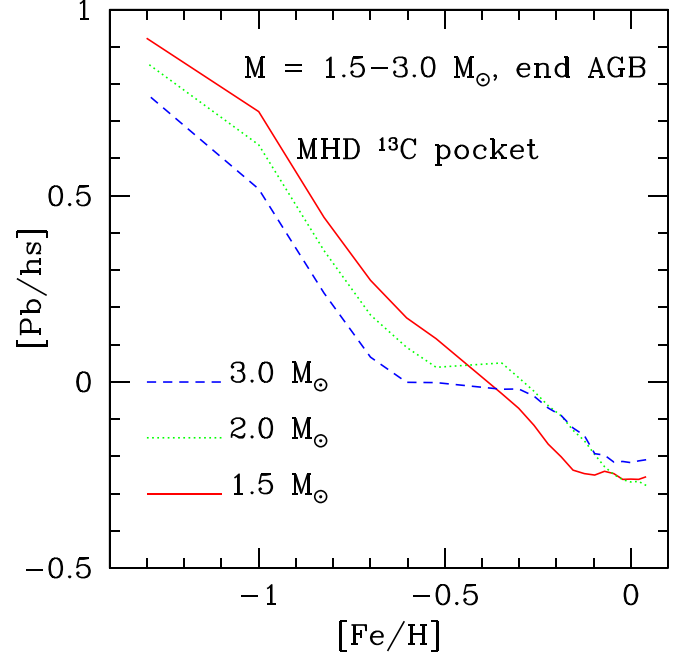


Figure 11. Relative production factors for Pb and for elements at the abundance peak near the magic neutron number $N = 82$, as summarized by the $[\text{Pb}/\text{hs}]$ indicator, for stellar masses $M = 1.5, 2.0$ and $3.0 M_{\odot}$ at various metallicities.

SFR from Maiorca et al. (2012). The result, once normalized to 1 for the average production factor of s -only nuclei, is presented in Table 3 and in Figure 14. This figure shows that the solar abundances of s -only nuclei are reproduced at a sufficient level of accuracy. There is in fact a slight asymmetry, a sort of minor deficit of s -only nuclei below $A \simeq 130$ with respect to the average distribution, which was sometimes found previously and was ascribed to an unknown *primary* nucleosynthesis process integrating neutron captures (Travaglio et al. 2004). However, in our results the asymmetry remains within the relatively small limits set by abundance and nuclear uncertainties, so that no real conclusion in favor of possible different nuclear processes can be drawn from our findings, confirming the previous indications by Maiorca et al. (2011), Cristallo et al. (2015a), Prantzos et al. (2018)

The detailed s -process fractions that are listed in Table 3 can then be used to disentangle the s and r contributions to each isotope, as done (for example) by Arlandini et al. (1999), Prantzos et al. (2020). Since the table contains predictions for fractional contributions to each isotope from the s -process Main Component, the maximum ratio that one should get is obviously one, reserved to s -only isotopes that do not receive contributions from other components (i.e., those in the atomic mass range between about 90 and about 210). As Table 3

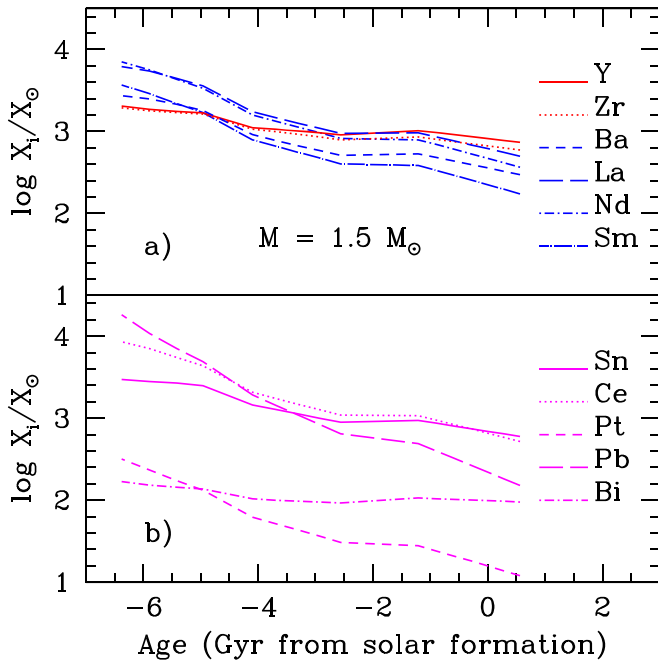


Figure 12. Production factors of representative neutron-rich elements in stellar models of $1.5 M_\odot$, for varying metallicities and Galactic ages, using the Age–Metallicity relation mentioned in the text. The elements at the first (red) and second (blue) s -process peak (panel (a)) remain remarkably similar for a rather long time in the Galactic evolution that preceded solar formation (roughly between -4 and -1.5 Gyr). This is not true for the other elements (panel (b)), in particular, Pb has the peculiar trend of increasing steadily for decreasing metallicity.

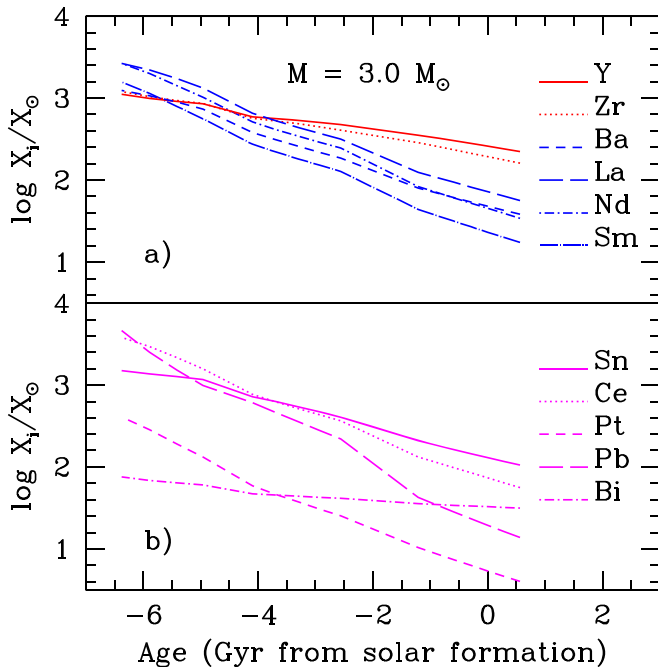


Figure 13. Same as in Figure 12, for models of $3.0 M_\odot$. Here the stationary behavior shown in panel (a) of the previous figure is not present, if not for a shorter time interval at earlier ages.

shows, this is not formally true, with the fractional productions slightly differing from unity. One can, however, notice that the global value of the variance in the distribution ($\sigma \lesssim 15\%$) is in the range of general uncertainties known to exist on the product

of the two sets of crucial parameters, solar abundances (N_i) and cross sections (σ_{N_i}); the limited residual problems can therefore be simply due to the effects of these uncertainties in the input data. It is in any case worth noticing the cases of two special nuclei in Table 3. The first isotope that we want to mention is ^{152}Gd , which is sometimes indicated as an s -only isotope, whose production in our scenario amounts only to about 60% of its solar concentration. In fact, we restrain from considering ^{152}Gd as a real s -only isotope because it is not shielded against β^+ decays and might receive a high contribution from the p -process. The second nucleus is ^{93}Nb , which is produced at 66% of its solar abundance. It is not shielded against β -decays, so that its production can be partially due also to the p -process, through ^{93}Mo (β^+ , $t_{1/2} \simeq 4000$ yr) and to the r -process, through ^{93}Zr (β^- , $t_{1/2} \simeq 1.5$ Myr). In evolved stars, its presence is normally seen in objects enriched by mass transfer from an AGB companion (i.e., in Ba-stars and their relatives, see Section 4.2). It must, however, be noticed that a further source for ^{93}Nb production can arise if a Ba-star evolves in its turn to the TP-AGB phase, thus undergoing s -enrichment for a second time. Such a phenomenon is in fact observed (Shetye et al. 2020); detailed computations in this last scenario will be necessary for determining the real s -process contribution to ^{93}Nb .

4. Constraints from Presolar Grains and Evolved Stars

The surface stellar abundances that were derived in the previous sections can be compared with various constraints deriving either from spectroscopic observations of evolved stars or from the analysis of presolar grains of AGB origin (primarily of the SiC grain family, see Lodders & Fegley 1995; Davis 2011). For both these fields, a detailed and critical description of the database used would be necessary, implying a rather long analyses that cannot be pursued here. Therefore, we simply anticipate here some relevant examples, postponing more detailed analyses to separate contributions.

4.1. Crucial Isotopic Ratios in Presolar SiC Grains

For presolar grains, results based on a preliminary extension of Paper II, similar albeit more limited than the present one, were shown in Palmerini et al. (2018). We refer to that paper for most of the details. Here, we want to emphasize that a few isotopic ratios of trace elements measured recently in presolar SiC grains were crucial for excluding some previous parameterized scenarios for the formation of the ^{13}C source. They were also used to suggest that models based on the indications contained in Paper II had instead the characteristics that are required to account for the grain data (Liu et al. 2015, 2018). These measurements are therefore important tests to validate nucleosynthesis results deriving from any specific mixing scheme because other general constraints on s -processing are much less sensitive to the details of mixing (Buntain et al. 2017). Of particular importance in this respect is the isotopic ratio $^{92}\text{Zr}/^{94}\text{Zr}$ versus $^{96}\text{Zr}/^{94}\text{Zr}$ (Liu et al. 2014), as well as the correlation between $^{88}\text{Sr}/^{86}\text{Sr}$ and $^{138}\text{Ba}/^{136}\text{Ba}$ (Liu et al. 2015, 2018). These data (expressed in the usual δ notation) are reproduced in Figures from 16–19, which are overimposed to our model sequences (see the discussion that follows).

The choice of what to define as carbon-enhanced composition requires some comments. SiC grains are carbon-rich

Table 3
Percentages from the *s*-process Main Component

A	Elem.	Perc. MC	A	Elem.	Perc. MC	A	Elem.	Perc. MC	A	Elem.	Perc. MC
58	Fe	0.031	63	Cu	0.014	64	Ni	0.047	64	Zn	0.006
65	Cu	0.038	66	Zn	0.026	67	Zn	0.037	68	Zn	0.059
69	Ga	0.083	70	Ge	0.132	70	Zn	0.005	71	Ga	0.129
72	Ge	0.135	73	Ge	0.087	74	Ge	0.137	75	As	0.088
76	Se	0.213	76	Ge	0.001	77	Se	0.092	78	Se	0.145
79	Br	0.116	80	Kr	0.159	81	Br	0.142	82	Kr	0.409
82	Se	0.001	83	Kr	0.131	84	Kr	0.123	85	Rb	0.140
86	Kr	0.207	86	Sr	0.776	87	Rb	0.195	87	Sr	0.781
88	Sr	0.915	89	Y	0.843	90	Zr	0.664	91	Zr	0.780
92	Zr	0.757	93	Nb	0.660	94	Zr	0.976	95	Mo	0.495
96	Mo	1.033	96	Zr	0.106	97	Mo	0.564	98	Mo	0.750
99	Ru	0.262	100	Ru	1.021	101	Ru	0.160	102	Ru	0.430
103	Rh	0.130	104	Pd	1.078	104	Ru	0.012	105	Pd	0.139
106	Pd	0.510	107	Ag	0.015	108	Pd	0.622	109	Ag	0.241
110	Cd	0.975	110	Pd	0.014	111	Cd	0.231	112	Cd	0.493
113	Cd	0.342	114	Cd	0.614	115	In	0.352	116	Sn	0.874
116	Cd	0.059	117	Sn	0.494	118	Sn	0.727	119	Sn	0.395
120	Sn	0.811	121	Sb	0.376	122	Te	0.901	122	Sn	0.350
123	Te	0.953	123	Sb	0.042	124	Sn	0.002	124	Te	0.967
125	Te	0.224	126	Te	0.453	127	I	0.048	128	Xe	0.974
128	Te	0.022	129	Xe	0.038	130	Xe	1.011	130	Te	0.001
131	Xe	0.078	132	Xe	0.403	133	Cs	0.157	134	Ba	0.923
134	Xe	0.024	135	Ba	0.055	136	Ba	0.955	136	Xe	0.001
137	Ba	0.122	138	Ba	0.185	139	La	0.784	140	Ce	0.979
141	Pr	0.545	142	Nd	1.166	142	Ce	0.084	143	Nd	0.372
144	Nd	0.575	145	Nd	0.292	146	Nd	0.734	147	Sm	0.231
148	Sm	1.121	148	Nd	0.093	149	Sm	0.141	150	Sm	1.039
150	Nd	0.000	151	Eu	0.090	152	Gd	0.611	152	Sm	0.243
153	Eu	0.053	154	Gd	1.250	154	Sm	0.005	155	Gd	0.064
156	Gd	0.191	157	Gd	0.127	158	Gd	0.033	159	Tb	0.078
160	Dy	1.140	160	Gd	0.006	161	Dy	0.059	162	Dy	0.166
163	Dy	0.036	164	Dy	0.169	165	Ho	0.085	166	Er	0.159
167	Er	0.095	168	Er	0.313	169	Tm	0.145	170	Yb	1.210
170	Er	0.044	171	Yb	0.156	172	Yb	0.352	173	Yb	0.271
174	Yb	0.581	175	Lu	0.181	176	Lu	1.219	176	Hf	0.930
176	Yb	0.040	177	Hf	0.167	178	Hf	0.572	179	Hf	0.422
180	Hf	0.983	181	Ta	0.907	182	W	0.696	183	W	0.665
184	W	0.744	185	Re	0.251	186	Os	1.102	186	W	0.277
187	Re	0.033	187	Os	0.492	188	Os	0.262	189	Os	0.042
190	Os	0.125	191	Ir	0.019	192	Os	0.009	192	Pt	0.999
193	Ir	0.013	194	Pt	0.049	195	Pt	0.020	196	Pt	0.117
197	Au	0.060	198	Hg	1.210	198	Pt	0.000	199	Hg	0.210
200	Hg	0.511	201	Hg	0.391	202	Hg	0.661	203	Tl	0.775
204	Pb	1.050	204	Hg	0.102	205	Tl	0.711	206	Pb	0.660
207	Pb	0.748	208	Pb	0.491	209	Bi	0.066			

solids, so their formation is normal for an abundance ratio C/O larger than unity. However, recent work on non-equilibrium chemistry in circumstellar envelopes suggests that the contemporary formation of both O-rich and C-rich molecules can occur for wide composition ranges of the environment thanks to various complex phenomena, including the photodissociation and re-assembly of previously formed compounds. According to Cherchneff (2006), a two-component (silicate-carbon) dust may form when the C/O ratio is sufficiently high, even before it formally reaches unity, along the AGB evolution. These suggestions correspond to the observations by Olofsson et al. (1998), who found carbon-rich compounds (like the HCN molecule) in O-rich environments. Therefore, we allowed a more relaxed constraint to the carbon enrichment of the envelope, imposing that C/O be larger than 0.8.

The composition of the envelope is largely influenced by mass loss rates, whose understanding is far from satisfactory. As mentioned before in this note, we can avoid being dominated by uncertainties in stellar wind efficiency if we use the composition of the $G - component$ in addition to the envelope composition. The importance of the $G - component$ is enhanced by the already-mentioned fact that this extrapolated phase mimics well the abundances in flux tubes at each TDU episode, hence also that of possible flare-like phenomena disrupting magnetic structures in the winds and adding C-rich materials to them.

Figures from 16 to 19 are therefore plotted in two panels: one representing the formal envelope composition when a C-rich situation ($C/O > 0.8$) has been reached, and the second showing the pure, C-rich G -component. It is clear that from the

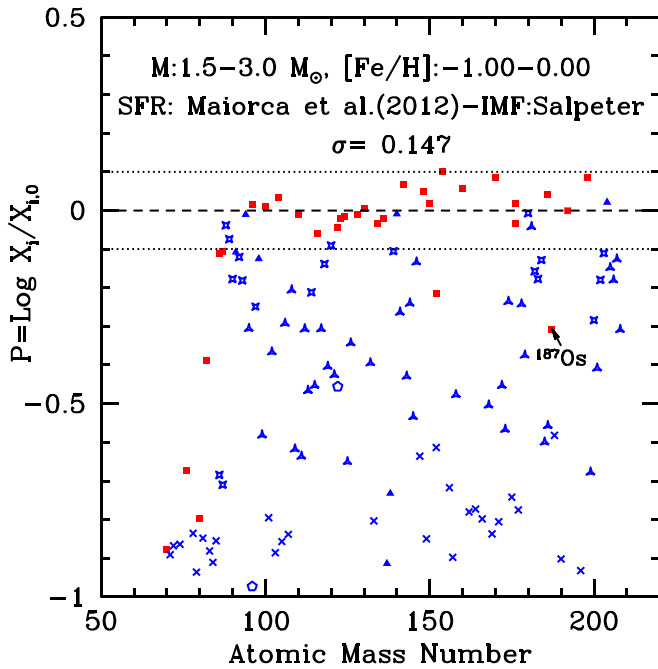


Figure 14. Simulation of the chemical admixture operated by Galactic evolution, obtained by weighting our model abundances over a Salpeter IMF and a SFR taken from Maiorca et al. (2012). Symbols and colors have the same meaning as in Figure 4.

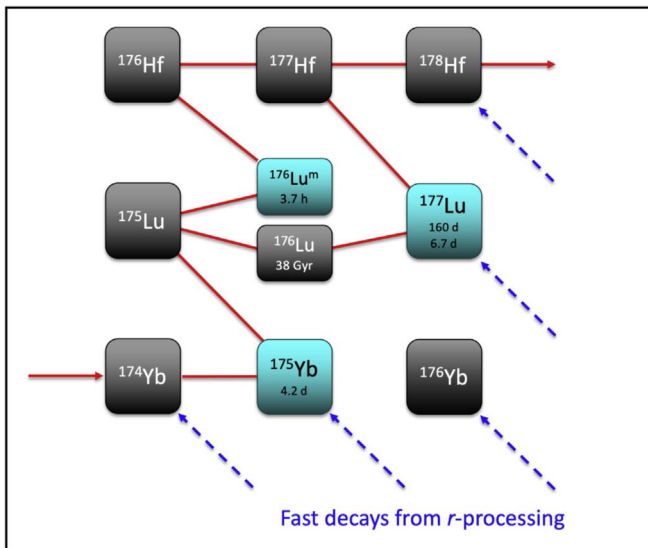


Figure 15. The neutron-capture path around ^{176}Lu and ^{176}Hf in the chart of the nuclei, when the isomeric state and the ground state of ^{176}Lu are not thermalized. See text for comments.

figures that at least this last offers excellent possibilities of reproducing the presolar grain data for critical Sr, Zr and Ba isotopic ratios, which confirms the viability of the adopted choices for the partial mixing processes generating the ^{13}C -pocket and is in agreement with the mentioned findings by Liu et al. (2015, 2018). We notice here that accounting for measurements with $\delta(^{92}\text{Zr}/^{94}\text{Zr}) \geq -50$ was considered as impossible for s -process modeling (Lugaro et al. 2014). In Liu et al. (2014, 2015) it was underlined how the problem could be alleviated or bypassed through a specific parameterization of the ^{13}C pocket, subsequently recognized to mimic the

distribution found in our Paper II (Liu et al. 2018). Here, Figures 16 and 17 better specify the reason of this way out. The puzzling isotopic ratios correspond roughly to our G - component at the first TDU episodes for high metallicity stars. The explanation of this is straightforward: in early cycles of high metallicity models, still at low temperature and having a low neutron density in the pulses, ^{96}Zr is essentially destroyed, while a marginal production of ^{92}Zr occurs. Clearly, the envelope is still O-rich, but for us (as already mentioned) the G - component mimics rather well the composition of those flux tubes that, surviving disruption in the turbulent convective envelope, reach the surface (as done by the solar magnetic structures forming the corona). When a few magnetized blobs reach the atmosphere without mixing, kept together by magnetic tension, the solids that are condensed there have a finite probability of preserving a C-enriched composition, being contemporarily slightly ^{92}Zr -rich and largely ^{96}Zr -poor. Therefore, we believe that presolar SiC grains, through those isotopic ratios that are otherwise hardly associated to C-rich envelopes, add a remarkable piece of evidence in favor of our MHD mixing scheme, naturally accounting for the existence C-rich blobs, where carbon-based dust can be formed even during generally O-rich phases.

In Figures 16 and 17, the few points at high, positive values of $\delta(^{92}\text{Zr}/^{94}\text{Zr})$ and with $\delta(^{96}\text{Zr}/^{94}\text{Zr}) \geq -500$, which are not covered by the region of the models, might be easily fitted should one consider initial abundance ratios for Zr isotopes in the envelope different from solar. This would indeed be the case for stellar models of low metallicity because the contributions from AGB stars to the lighter isotopes of Zr is lower (see Table 3) than for the reference ^{94}Zr , implying that the envelope (initial) δ value for (say) $^{92}\text{Zr}/^{94}\text{Zr}$ should be slightly higher than zero. We believe, however, that one should restrain from over-interpreting the data: there are, in fact, remaining problems in them that hamper too strong conclusions and suggest the need for new high-precision measurements. This was extensively discussed in Liu et al. (2018), to which we refer for details. We also remind the reader that important effects on the Zr isotopes of SiC grains, related to the composition of the parent stars and also invoking contributions from super-solar-metallicity AGBs, were suggested by Lugaro et al. (2018). This possibility and other relevant issues on this subject will be discussed in more detail in a separate, forthcoming paper.

4.2. Reproducing the Abundances of AGB Stars and their Relatives

AGBs are in principle also precious because, thanks to the TDU episodes, they offer a unique opportunity to observe ongoing nucleosynthesis products directly in the producing stars. Several important observational studies on their O-rich and C-rich members exist, and they have been crucial in revealing their properties and composition (Smith & Lambert 1985, 1986, 1990; Busso et al. 1992, 2001; Smith et al. 1995; Abia 2008; Abia et al. 2008, 2015, 2017, 2020; Rau et al. 2017; Shetye et al. 2018). However, due to their low temperature and complex atmospheric dynamics, they become very difficult to observe when they cross their final (TP) phases. At long wavelengths, in their cool circumstellar envelopes, n -capture elements are easily condensed at relatively low temperatures (Ritchey et al. 2018). Consequently, the abundances measured for the gaseous phase are difficult to correlate with the atmospheric ones. Meanwhile, these atmospheres are subject to strong radial pulsations, with periods of the order of

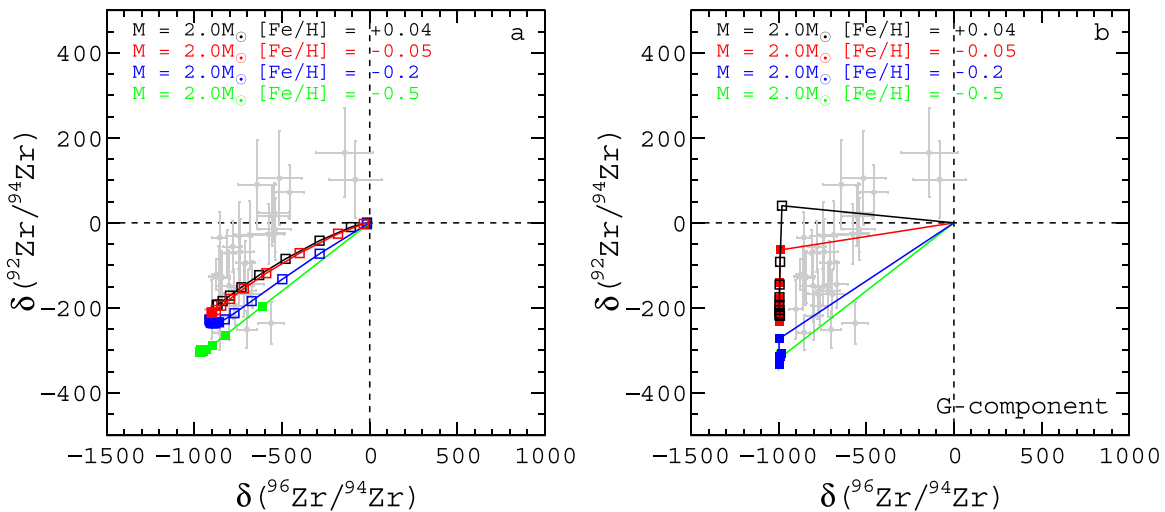


Figure 16. The isotopic ratios $^{92}\text{Zr}/^{94}\text{Zr}$ measured in presolar SiC grains, vs. $^{96}\text{Zr}/^{94}\text{Zr}$, in δ units, taken from the measurements cited in the text. They are compared with our model sequences for stellar atmospheres (left-hand panel) and for the *G* – component (right-hand panel), for stars of $M = 2 M_{\odot}$. Lower masses would not differ much from the plot shown, if not for the more limited extension of the C-rich phase.

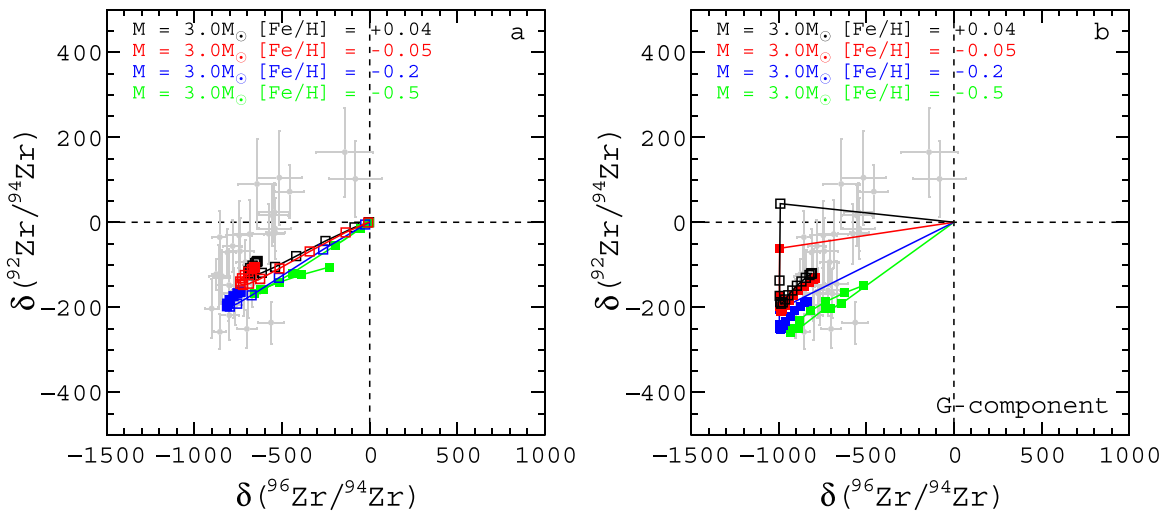


Figure 17. Same as in Figure 16, but for model stars of $M = 3 M_{\odot}$.

one year (from a fraction to a few), which make them variable by several magnitudes (LPVs, or Long Period Variables), see for example Wood & Sebo (1996). They are classified as being Mira or Semi-regular pulsators, with pulsations that are variously dominated by the fundamental or first overtone mode (Wood 1990). Model atmospheres in those conditions are extremely complex (see Höfner et al. 2000; Gautschy-Loidl et al. 2004, and citations there). Moreover, strong molecular transitions hamper the observations of crucial elements (Abia et al. 2008). Owing to these difficulties, various families of relatives (having warmer photospheres) have become important surrogates in providing information on AGB nucleosynthesis. In particular, this includes binary systems where a surviving companion inherited measurable abundances of *n*-capture elements through mass transfer by a specific mechanism, which is called *wind accretion* (Boffin & Jorissen 1988; Jorissen & Mayor 1992). The elements that were formed previously in an AGB star now generally evolved to the white dwarf phase (see, e.g., Jorissen et al. 1998, 2005; Escorza et al. 2019a, 2019b, 2020, and references quoted therein). These objects are often called *extrinsic* AGBs (Smith & Lambert 1988;

Jorissen & Mayor 1992), the most famous class being that of classical Ba-II stars. These stars have been the object of many studies over the years, and of recent extensive discussions, with new observational data; see for example Jorissen et al. (2019). Although we cannot afford such an extended topic in detail here, we need at least to verify our models in general on Ba-star constraints.

Another class of AGB relatives that attracted large attention are post-AGB objects that in their evolution toward the white dwarf stage cross blueward the HR diagram, heating their remaining envelope and passing therefore through various spectral types corresponding to temperatures warmer than for real AGB stars (Reyniers & Van Winckel 2003; van Winckel 2003a, 2003b; Reyniers et al. 2004; De Smedt et al. 2012, 2015a). This class also includes extrinsic objects (Kamath 2019; Kamath & Van Winckel 2019). We need here to present at least a couple of examples of how our model scenario compares with post-AGB constraints.

Starting with Ba-stars, extended fits to some of their abundance distributions were made by us many years ago

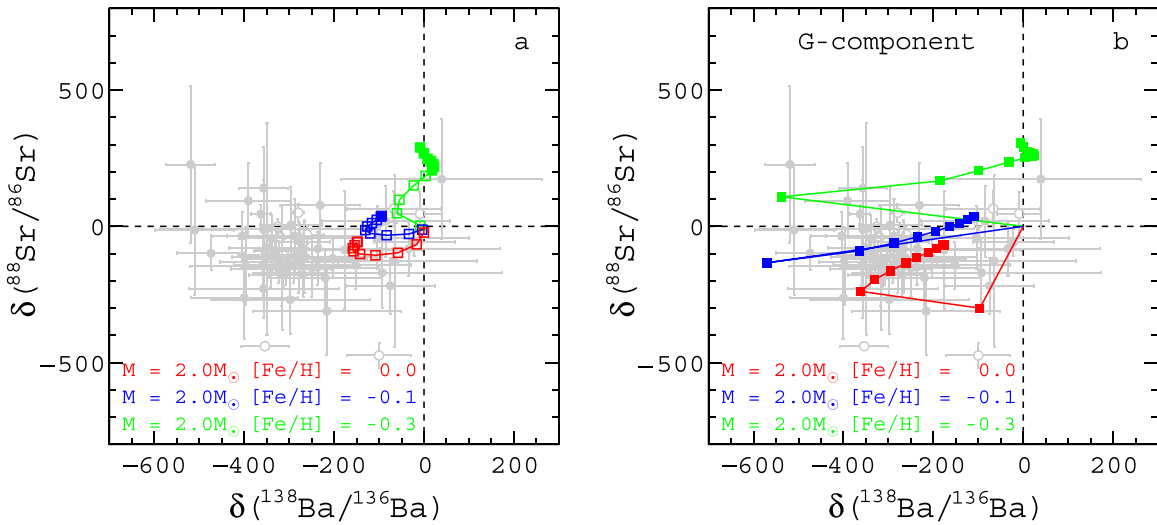


Figure 18. The isotopic ratios $^{88}\text{Sr}/^{86}\text{Sr}$ observed in presolar SiC grains, vs. $^{138}\text{Ba}/^{136}\text{Ba}$, expressed with the δ notation, taken from the measurements cited in the text, as compared with our model sequences for stellar atmospheres (left-hand panel) and for the *G* – component (right-hand panel) of stars with $M = 2.0 M_{\odot}$. Again, lower mass models do not differ drastically from what is shown. The data are integrated, with respect to Palmerini et al. (2018) with those shown by Liu et al. (2017); Stephan et al. (2018).

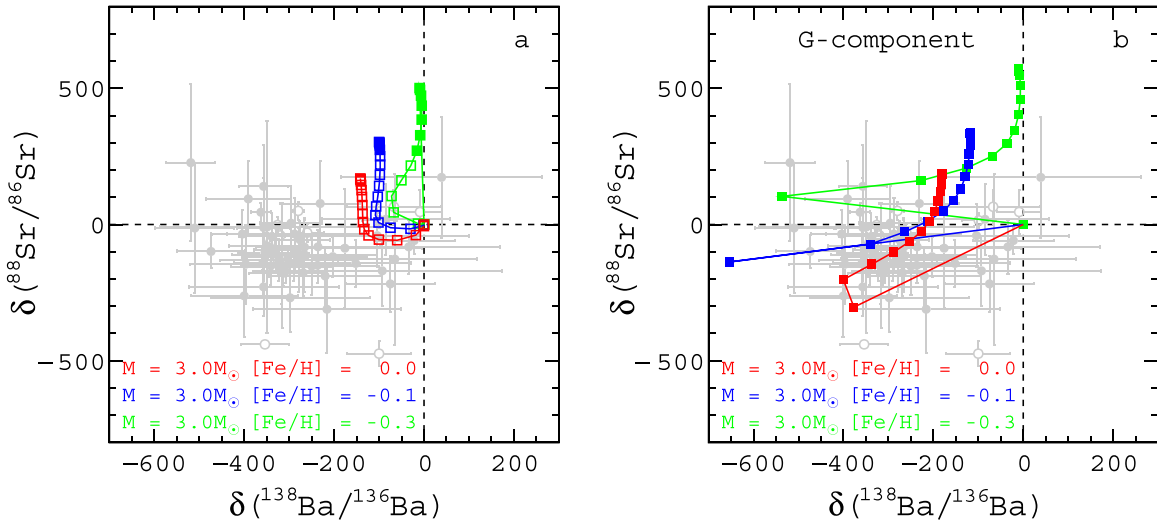


Figure 19. Same as in Figure 18, but for model stars of $M = 3 M_{\odot}$.

(Busso et al. 1995, 2001) as a tool for understanding the extensions of the ^{13}C pockets by calibrating parameterized models on observations. An example of how things have changed now is shown in Figure 20, for HR774 (HD 16458), whose abundances are taken from the measurements by Tomkin & Lambert (1983) and by Smith (1984). Our original fitting attempt was presented in Table 2 and Figure 12 of Busso et al. (1995) for two tentative parameterized models. Figure 20 shows the comparison of one such model (model B) with what can be obtained in the envelope of a low mass star, of metallicity $[\text{Fe}/\text{H}] = -0.6$, having undergone efficient mass transfer from an AGB companion of about $1.5 M_{\odot}$. The two model curves, albeit different, are fully compatible with the observed data; what 25 yr ago could only be obtained by fixing ad-hoc the parameters (in particular the abundance of ^{13}C burnt), is now a natural outcome of our scenario with MHD mixing, applied to the mentioned star and without adjusting any further parameter. We might choose several other examples. In most cases, the observations do not include as

many *s*-elements as for HR774, but they have reached a considerable statistical extension and are made with more modern instrumentation. Two such examples are shown in Figure 21, taken from the samples by de Castro et al. (2016) and by Jorissen et al. (2019). We choose the star BD-14 $^{\circ}$ 2678 from the first mentioned list, and HD27271 from the second one. In this last case, the observations are from Karinkuzhi et al. (2018), who also measured the critical element Nb, having only one stable isotope, ^{93}Nb . As mentioned, this nucleus is produced by decay of the rather long-lived parent ^{93}Zr and the presence of the daughter ^{93}Nb is a clear indication that the star is extrinsic. Both the chosen sources are classified as mild Ba-stars by Jorissen et al. (2019).

The examples that are shown in the figure represent rather typical cases and the quality of the fits is in general good. However, this is not possible for *all* Ba-stars because some of the available datasets contain individual elements with abundances that are incompatible with any *s*-process distribution, such as elements belonging to one of the major abundance

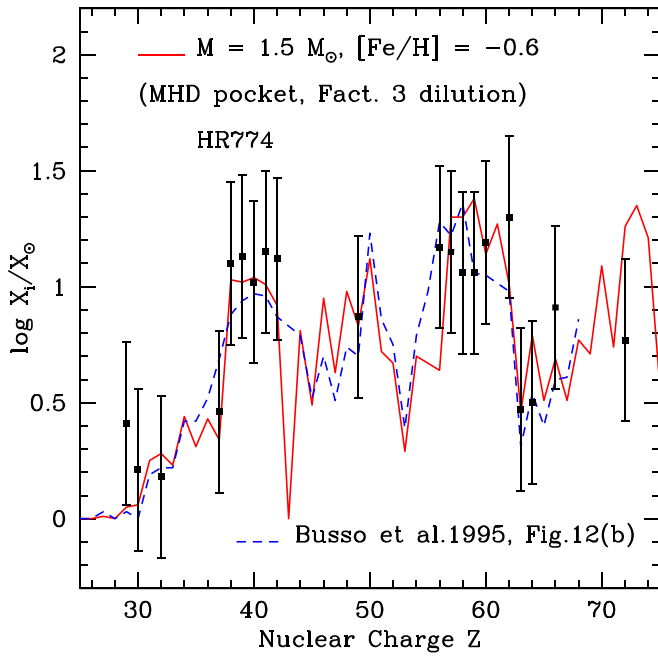


Figure 20. Comparison of models with observations for the Ba-star HR774. We show results from the present work (red continuous line) as well as from the parametric study by Busso et al. (1995), namely their case B (blue dashed line).

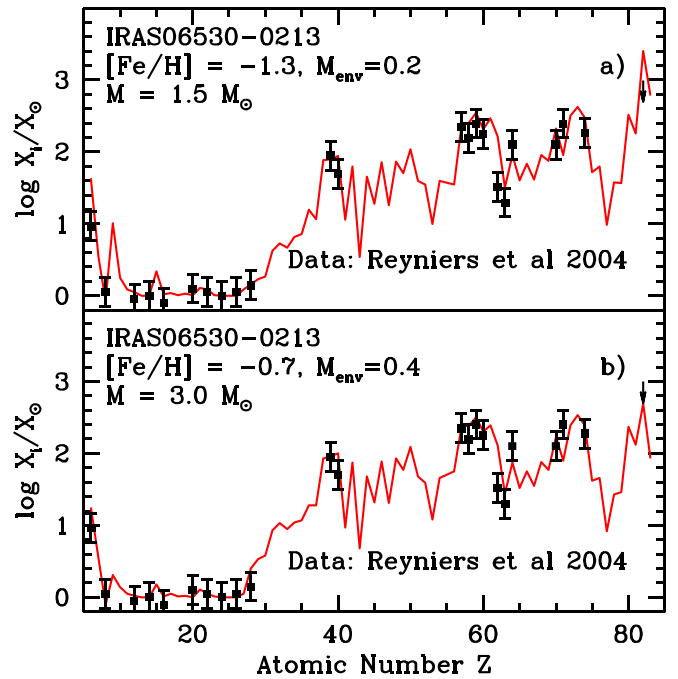


Figure 22. Comparison of our model results with the observations for the post-AGB star IRAS06530-0213. The curve of panel (a), from a low mass star, shows the usual discrepancy on the abundance of Pb, which can in this case be avoided with a fit taken from a more massive star and a higher metallicity (panel (b)).

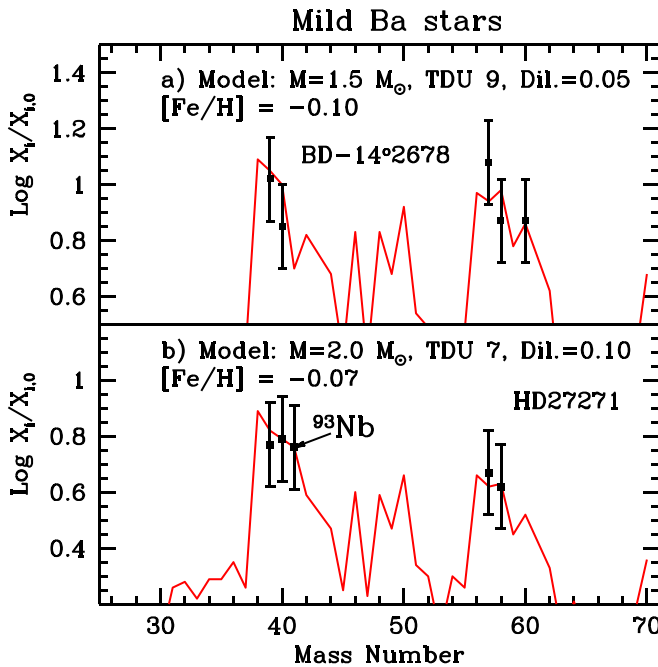


Figure 21. Comparison of our models with observations for two mild Ba-stars (see text for details)

peaks, which are discrepant by large amounts (even one order of magnitude) with respect to their neighbors. Although the origin of these discrepancies is not known, we believe they may be due to difficulties in spectroscopic observations. We must in this respect remind the reader that the cases that are shown here derive from a very simple approach to mass accretion (actually, a simple dilution of the AGB material). More sophisticated treatments exist and should in fact be pursued, as done in some cases in the past (Stancliffe & Glebbeek 2008).

An important signature of how s -elements are enriched over the galactic history is provided by the abundance of Pb, whose trend is shown here in Figure 11, and roughly the same behavior was previously found by all groups working in the field: see for example Gallino et al. (1998), Goriely & Mowlavi (2000), Lugaro et al. (2012). As mentioned, the increase in the neutron exposure for lower abundance of the seeds makes it unavoidable that, on average, the photospheric abundance expected for Pb increases toward lower metallicities. While most observations of metal-poor extrinsic AGB stars confirmed this evidence, some of them did not (Aoki et al. 2001; Van Eck et al. 2001, 2003; Behara et al. 2010; Bisterzo et al. 2012). This throws a shadow on our understanding of the s -process scenario, which is robust for the rest. More doubts on Pb were accumulated in recent years from the second sample of AGB relatives we mentioned (i.e., that of post-AGB stars), which again for the rest confirmed the known trend of s -enrichment with metallicity (De Smedt et al. 2014). In the last two decades, various observational studies and detailed analyses have been performed in this framework. We refer to known works in this field, such as Reyniers & Van Winckel (2003), Reyniers et al. (2004, 2007), De Smedt et al. (2012, 2015a, 2015b, 2016) and to review papers such as van Winckel (2003a, 2003b) for general reference on the subject. Both for Galactic (De Smedt et al. 2016) and for extra-galactic low-metallicity post-AGB stars (De Smedt et al. 2014), the expected strong enhancement of Pb was found not to be compatible with the upper limits determined observationally. Even if these indications should be confirmed, the Pb problem would remain in our models; as shown for example in Figure 22, panel (a), for observations by Reyniers et al. (2004). This can be sometimes avoided if we refer to stellar models of $3 M_{\odot}$ (see panel (b)) as, in our scenario, the s -process efficiency decreases in general for

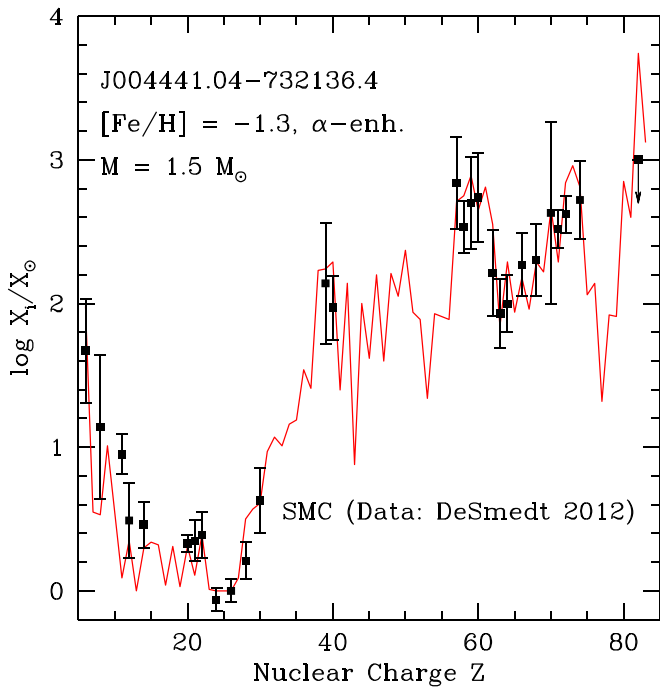


Figure 23. Comparison of our model results with the observations for the post-AGB star J004441.04–732136.4. See text for details.

increasing stellar mass. However, the star shown seems to be of lower mass and metallicity than found in this purely formal solution (Hrivnak & Reddy 2003). We notice, in any case, how Figure 22 shows that the remaining abundance distribution is reproduced quite well, at the same level that was only previously possible through models with parameterized extra-mixing. A similar situation emerges from the comparison in Figure 23, which was done with the observations of the low-mass post-AGB star J004441.04–732136.4 in the Small Magellanic Cloud (SMC) by De Smedt et al. (2012, 2014). This star is also classified as a Carbon-Enhanced Metal-Poor star, enriched in both r - and s -elements (CEMP $r-s$, see Cui et al. 2014). We recall how these objects often pose very difficult problems to detailed modeling of their abundances (Stancliffe & Lugaro 2012). Very recently, new HST ultraviolet observations of three metal-poor stars by Roederer et al. (2020), using for the first time the Pb II line at $\lambda = 220.35$ nm, yielded much higher abundances for Pb (by 0.3–0.5 dex) than previously found with Pb I lines. The authors suggest that these last may lead to underestimate the Pb abundance. Although it is premature to derive final conclusions from such suggestions, they may open the road for solving a long-lasting discrepancy between observations and nucleosynthesis computations for AGB stars and their relatives, thus also reconciling our models with the measured data.

5. Conclusions

The results of this work can be summarized by saying that we have shown how a general scenario for the activation of the ^{13}C neutron source in AGB stars can be built on the simple hypothesis that the required mixing processes derive from the activation of a stellar dynamo, in which an exact, *particular* solution to MHD equations is possible on the basis of the simple but plausible average field geometry that was suggested by Nucci & Busso (2014).

In particular, we have shown how, based on that hypothesis, one can avoid all further free parameterizations and deduce rather general rules for deriving the extensions and shapes of the ^{13}C distributions left in the He-intershell zone at each TDU episode. These distributions provide nucleosynthesis models that are suitable to explain the known observational constraints on s -processing. These last include the average s -element distribution in our solar system, as well as the peculiarities emerging from the isotopic ratios of trace elements measured in presolar SiC grains. We show in this respect that some such ratios, that previously hardly accounted for by s -process models can be naturally explained if the cool winds of evolved low mass stars contain unmixed blobs of materials, which are transported by flux tubes above the convective envelope, such as occurs in the Sun. This hypothesis provides an approximate interpretation for the so-called G -component of AGB s -processing.

Our results also imply a scheme for the enrichment of neutron-capture elements in the Galaxy that accounts for most abundance observations of evolved low- and intermediate-mass stars, and has the characteristics previously indicated in the literature as required for understanding the enhanced heavy-element abundances of young open clusters.

As a consequence of our rather long reanalysis of the mixing processes required for making the neutron source ^{13}C available in the late-evolutionary stages of red giant stars, which was initiated with the studies by Busso et al. (2007), and considering that the observational confirmations that have been accumulated so far give us a sufficient guarantee of robustness, the mixing scheme that has developed in the past years has now been released for direct inclusion in full stellar models of the FUNS series (Cristallo et al. 2009, 2015b). A first attempt for implementing this integration was recently published separately by Vescovi et al. (2020).

ORCID iDs

Maurizio Busso <https://orcid.org/0000-0001-8944-5820>
 Diego Vescovi <https://orcid.org/0000-0003-0309-4666>
 Sara Palmerini <https://orcid.org/0000-0001-5386-8389>
 Sergio Cristallo <https://orcid.org/0000-0001-9683-9406>
 Vincenzo Antonuccio-Delogu <https://orcid.org/0000-0003-0630-9490>

References

- Abia, C. 2008, *AJ*, 136, 250
 Abia, C., Busso, M., Gallino, R., et al. 2001, *ApJ*, 559, 1117
 Abia, C., Cunha, K., Cristallo, S., & de Laverny, P. 2015, *A&A*, 581, A88
 Abia, C., de Laverny, P., Cristallo, S., Kordopatis, G., & Straniero, O. 2020, *A&A*, 633, A135
 Abia, C., de Laverny, P., & Wahlin, R. 2008, *A&A*, 481, 161
 Abia, C., Domínguez, I., Gallino, R., et al. 2002, *ApJ*, 579, 817
 Abia, C., Domínguez, I., Gallino, R., et al. 2003, *PASA*, 20, 314
 Abia, C., Hedrosa, R. P., Domínguez, I., & Straniero, O. 2017, *A&A*, 599, A39
 Aoki, W., Ryan, S. G., Norris, J. E., et al. 2001, *ApJ*, 561, 346
 Arlandini, C., Käppeler, F., Wisshak, K., et al. 1999, *ApJ*, 525, 886
 Battino, U., Pignatari, M., Ritter, C., et al. 2016, *ApJ*, 827, 30
 Battino, U., Tattersall, A., Lederer-Woods, C., et al. 2019, *MNRAS*, 489, 1082
 Behara, N. T., Bonifacio, P., Ludwig, H. G., et al. 2010, *A&A*, 513, A72
 Bisterzo, S., Gallino, R., Straniero, O., Cristallo, S., & Käppeler, F. 2012, *MNRAS*, 422, 849
 Boffin, H. M. J., & Jorissen, A. 1988, *A&A*, 205, 155
 Boothroyd, A. I., Sackmann, I. J., & Wasserburg, G. J. 1995, *ApJL*, 442, L21
 Buntain, J. F., Doherty, C. L., Lugaro, M., et al. 2017, *MNRAS*, 471, 824
 Busso, M., Gallino, R., Lambert, D. L., Raiteri, C. M., & Smith, V. V. 1992, *ApJ*, 399, 218

- Busso, M., Gallino, R., Lambert, D. L., Travaglio, C., & Smith, V. V. 2001, *ApJ*, **557**, 802
- Busso, M., Gallino, R., & Wasserburg, G. J. 1999, *ARA&A*, **37**, 239
- Busso, M., Lambert, D. L., Beglio, L., et al. 1995, *ApJ*, **446**, 775
- Busso, M., Palmerini, S., Maiorca, E., et al. 2010, *ApJL*, **717**, L47
- Busso, M., Wasserburg, G. J., Nollett, K. M., & Calandra, A. 2007, *ApJ*, **671**, 802
- Casali, G., Spina, L., Magrini, L., et al. 2020, *A&A*, **643**, A12
- Chandrasekhar, S. 1939, *An Introduction to the Study of Stellar Structure* (Chicago, IL: Univ. Chicago Press)
- Charbonnel, C., & Balachandran, S. C. 2000, *A&A*, **359**, 563
- Charbonnel, C., & Lagarde, N. 2010, *A&A*, **522**, A10
- Charbonnel, C., & Zahn, J.-P. 2008, in *IAU Symp. 252, The Art of Modeling Stars in the 21st Century*, ed. L. Deng & K. L. Chan (Cambridge: Cambridge Univ. Press), 245
- Cherchneff, I. 2006, *A&A*, **456**, 1001
- Cristallo, S., Abia, C., Straniero, O., & Piersanti, L. 2015a, *ApJ*, **801**, 53
- Cristallo, S., La Cognata, M., Massimi, C., et al. 2018, *ApJ*, **859**, 105
- Cristallo, S., Piersanti, L., Straniero, O., et al. 2011, *ApJS*, **197**, 17
- Cristallo, S., Straniero, O., Gallino, R., et al. 2009, *ApJ*, **696**, 797
- Cristallo, S., Straniero, O., Piersanti, L., & Gobrecht, D. 2015b, *ApJS*, **219**, 40
- Cui, W., Zhang, B., & Zhao, G. 2014, *SCPMA*, **57**, 1201
- Davis, A. M. 2011, *PNAS*, **108**, 19142
- de Castro, D. B., Pereira, C. B., Roig, F., et al. 2016, *MNRAS*, **459**, 4299
- De Smedt, K., Van Winckel, H., Kamath, D., et al. 2014, *A&A*, **563**, L5
- De Smedt, K., Van Winckel, H., Kamath, D., et al. 2015a, in *ASP Conf. Ser. 497, Why Galaxies Care about AGB Stars III: A Closer Look in Space and Time*, ed. F. Kerschbaum, R. F. Wing, & J. Hron (San Francisco, CA: ASP), 241
- De Smedt, K., Van Winckel, H., Kamath, D., et al. 2016, *A&A*, **587**, A6
- De Smedt, K., Van Winckel, H., Kamath, D., & Wood, P. R. 2015b, *A&A*, **583**, A56
- De Smedt, K., Van Winckel, H., Karakas, A. I., et al. 2012, *A&A*, **541**, A67
- Denissenkov, P. A., & Merryfield, W. J. 2011, *ApJL*, **727**, L8
- Denissenkov, P. A., & Tout, C. A. 2003, *MNRAS*, **340**, 722
- Dillmann, I., Heil, M., Käppeler, F., et al. 2006, in *AIP Conf. Ser. 819, Capture Gamma-Ray Spectroscopy and Related Topics*, ed. A. Woehr & A. Aprahamian (Melville, NY: AIP), 123
- Dillmann, I., Szücs, T., Plag, R., et al. 2014, *NDS*, **120**, 171
- Eggleton, P. P., Dearborn, D. S. P., & Lattanzio, J. C. 2006, *Sci*, **314**, 1580
- Eggleton, P. P., Dearborn, D. S. P., & Lattanzio, J. C. 2008, *ApJ*, **677**, 581
- Ekström, S., Georgy, C., Eggenberger, P., et al. 2012, *A&A*, **537**, A146
- Escorza, A., Boffin, H. M. J., Jorissen, A., et al. 2019a, *A&A*, **625**, C3
- Escorza, A., Karinkuzhi, D., Jorissen, A., et al. 2019b, *A&A*, **626**, A128
- Escorza, A., Siess, L., Van Winckel, H., & Jorissen, A. 2020, *A&A*, **639**, A24
- Freytag, B. 1996, in *ASP Conf. Ser. 108, M.A.S.S., Model Atmospheres and Spectrum Synthesis*, ed. S. J. Adelman, F. Kupka, & W. W. Weiss (San Francisco, CA: ASP), 93
- Gallino, R., Arlandini, C., Busso, M., et al. 1998, *ApJ*, **497**, 388
- Gallino, R., Busso, M., Picchio, G., Raiteri, C. M., & Renzini, A. 1988, *ApJL*, **334**, L45
- Gaustschy-Loidl, R., Höfner, S., Jørgensen, U. G., & Hron, J. 2004, *A&A*, **422**, 289
- Goriely, S., & Mowlavi, N. 2000, *A&A*, **362**, 599
- Heger, A., Langer, N., & Woosley, S. E. 2000, *ApJ*, **528**, 368
- Herwig, F. 2005, *ARA&A*, **43**, 435
- Herwig, F., Langer, N., & Lugaro, M. 2003, *ApJ*, **593**, 1056
- Höfner, S., Loidl, R., Aringer, B., Jørgensen, U. G., & Hron, J. 2000, in *ISO Beyond the Peaks 456, 2nd ISO Workshop on Analytical Spectroscopy*, ed. A. Salama et al. (Noordwijk: ESA-SP), 299
- Hrivnak, B. J., & Reddy, B. E. 2003, *ApJ*, **590**, 1049
- Huang, R. Q. 2004, *A&A*, **425**, 591
- Jorissen, A., Boffin, H. M. J., Karinkuzhi, D., et al. 2019, *A&A*, **626**, A127
- Jorissen, A., & Mayor, M. 1992, *A&A*, **260**, 115
- Jorissen, A., Van Eck, S., Mayor, M., & Udry, S. 1998, *A&A*, **332**, 877
- Jorissen, A., Začs, L., Udry, S., Lindgren, H., & Musaev, F. A. 2005, *A&A*, **441**, 1135
- Käppeler, F., Gallino, R., Busso, M., Picchio, G., & Raiteri, C. M. 1990, *ApJ*, **354**, 630
- Kamath, D. 2019, in *IAU Symp. 343, Why Galaxies Care About AGB Stars: A Continuing Challenge through Cosmic Time*, ed. F. Kerschbaum, M. Groenewegen, & H. Olofsson (Cambridge: Cambridge Univ. Press), 209
- Kamath, D., & Van Winckel, H. 2019, *MNRAS*, **486**, 3524
- Käppeler, F., Gallino, R., Bisterzo, S., & Aoki, W. 2011, *RvMP*, **83**, 157
- Käppeler, F., Winckler, N., Dababneh, S., et al. 2006, *MMSAI*, **77**, 916
- Karakas, A. I., & Lattanzio, J. C. 2014, *PASA*, **31**, e030
- Karinkuzhi, D., Van Eck, S., Jorissen, A., et al. 2018, *A&A*, **618**, A32
- Klay, N., Käppeler, F., Beer, H., et al. 1991a, *PhRvC*, **44**, 2801
- Klay, N., Käppeler, F., Beer, H., & Schatz, G. 1991b, *PhRvC*, **44**, 2839
- Kopp, G. 2016, *JSWSC*, **6**, A30
- Litvinov, Y. A., Bosch, F., Kozuharov, C., et al. 2011, *PhST*, **144**, 014001
- Liu, N., Gallino, R., Bisterzo, S., et al. 2014, *ApJ*, **788**, 163
- Liu, N., Gallino, R., Cristallo, S., et al. 2018, *ApJ*, **865**, 112
- Liu, N., Savina, M. R., Gallino, R., et al. 2015, *ApJ*, **803**, 12
- Liu, N., Stephan, T., Boehnke, P., et al. 2017, in *80th Annual Meeting of the Meteoritical Society*, **80**, 6283
- Lodders, K., & Fegley, B. J. 1995, *Metic*, **30**, 661
- Lodders, K., & Palme, H. 2009, *M&PS*, **72**, 5154
- Luck, R. E., & Bond, H. E. 1981, *ApJ*, **244**, 919
- Luck, R. E., & Bond, H. E. 1991, *ApJS*, **77**, 515
- Lugaro, M., Karakas, A. I., Petó, M., & Plachy, E. 2018, *GeCoA*, **221**, 6
- Lugaro, M., Karakas, A. I., Stancliffe, R. J., & Rijs, C. 2012, *ApJ*, **747**, 2
- Lugaro, M., Tagliente, G., Karakas, A. I., et al. 2014, *ApJ*, **780**, 95
- Maiorca, E., Magrini, L., Busso, M., et al. 2012, *ApJ*, **747**, 53
- Maiorca, E., Randich, S., Busso, M., Magrini, L., & Palmerini, S. 2011, *ApJ*, **736**, 120
- Mascali, D., Busso, M., Mengoni, A., et al. 2020, *EPJWC*, **227**, 01013
- Massimi, C., Aberle, O., Alcaayne, V., et al. 2019, in *Nuclei in the Cosmos XV*, ed. A. Formicola et al., Vol. 219 (New York: Springer), 63
- Matrozos, E., & Stancliffe, R. J. 2017, *A&A*, **606**, A55
- Mazzone, A., Cristallo, S., Aberle, O., et al. 2020, *PhLB*, **804**, 135405
- Nollett, K. M., Busso, M., & Wasserburg, G. J. 2003, *ApJ*, **582**, 1036
- Nordhaus, J., Busso, M., Wasserburg, G. J., Blackman, E. G., & Palmerini, S. 2008, *ApJL*, **684**, L29
- Nucci, M. C., & Busso, M. 2014, *ApJ*, **787**, 141
- Olofsson, H., Lindqvist, M., Nyman, L. A., & Winnberg, A. 1998, *A&A*, **329**, 1059
- Palmerini, S., Cristallo, S., Busso, M., et al. 2011, *ApJ*, **741**, 26
- Palmerini, S., Trippella, O., Busso, M., et al. 2018, *GeCoA*, **221**, 21
- Piersanti, L., Cristallo, S., & Straniero, O. 2013, *ApJ*, **774**, 98
- Pignatari, M., Herwig, F., Hirschi, R., et al. 2016, *ApJS*, **225**, 24
- Pinto, R. F., Brun, A. S., & Rouillard, A. P. 2016, *A&A*, **592**, A65
- Prantzos, N., Abia, C., Cristallo, S., Limongi, M., & Chieffi, A. 2020, *MNRAS*, **491**, 1832
- Prantzos, N., Abia, C., Limongi, M., Chieffi, A., & Cristallo, S. 2018, *MNRAS*, **476**, 3432
- Rau, G., Hron, J., Paladini, C., et al. 2017, *A&A*, **600**, A92
- Rauscher, T. 2012, *ApJL*, **755**, L10
- Reyniers, M., van de Steene, G. C., van Hoof, P. A. M., & van Winckel, H. 2007, *A&A*, **471**, 247
- Reyniers, M., & Van Winckel, H. 2003, *A&A*, **408**, L33
- Reyniers, M., Van Winckel, H., Gallino, R., & Straniero, O. 2004, *A&A*, **417**, 269
- Ritchie, A. M., Federman, S. R., & Lambert, D. L. 2018, *ApJS*, **236**, 36
- Roederer, I. U., Lawler, J. E., Holmbeck, E. M., et al. 2020, *ApJL*, **902**, L24
- Rosner, R. 1992, *AAS Meeting*, **181**, 59.02
- Rosner, R., An, C. H., Musielak, Z. E., Moore, R. L., & Suess, S. T. 1991, *ApJL*, **372**, L91
- Sabin, L., Wade, G. A., & Lèbre, A. 2015, *MNRAS*, **446**, 1988
- Salaris, M. 2007, in *AIP Conf. Ser. 948, Unsolved Problems in Stellar Physics: A Conference in Honor of Douglas Gough*, ed. R. J. Stancliffe et al. (Melville, NY: AIP), 87
- Salaris, M., & Cassisi, S. 2015, *A&A*, **577**, A60
- Schekochihni, A. A., Cowley, S. C., Taylor, S. F., Maron, J. L., & McWilliams, J. C. 2004, *ApJ*, **612**, 276
- Shetye, S., Goriely, S., Siess, L., et al. 2019, *A&A*, **625**, L1
- Shetye, S., Van Eck, S., Goriely, S., et al. 2020, *A&A*, **635**, L6
- Shetye, S., Van Eck, S., Jorissen, A., et al. 2018, *A&A*, **620**, A148
- Smith, V. V. 1984, *A&A*, **132**, 326
- Smith, V. V., & Lambert, D. L. 1985, *ApJ*, **294**, 326
- Smith, V. V., & Lambert, D. L. 1986, *ApJ*, **311**, 843
- Smith, V. V., & Lambert, D. L. 1988, *ApJ*, **333**, 219
- Smith, V. V., & Lambert, D. L. 1990, *ApJS*, **72**, 387
- Smith, V. V., Plez, B., Lambert, D. L., & Lubowich, D. A. 1995, *ApJ*, **441**, 735
- Söderlund, U., Patchett, P. J., Vervoort, J. D., & Isachsen, C. E. 2004, *E&PSL*, **219**, 311
- Soker, N., & Kastner, J. H. 2003, *ApJ*, **592**, 498
- Spitzer, L. 1962, *Physics of Fully Ionized Gases* (New York: Dover)
- Stancliffe, R. J. 2015, in *ASP Conf. Ser. 497, Why Galaxies Care about AGB Stars III: A Closer Look in Space and Time*, ed. F. Kerschbaum, R. F. Wing, & J. Hron (San Francisco, CA: ASP), 253

- Stancliffe, R. J., Dearborn, D. S. P., Lattanzio, J. C., Heap, S. A., & Campbell, S. W. 2011, [ApJ](#), **742**, 121
- Stancliffe, R. J., & Glebbeek, E. 2008, [MNRAS](#), **389**, 1828
- Stancliffe, R. J., & Jeffery, C. S. 2007, [MNRAS](#), **375**, 1280
- Stancliffe, R. J., & Lattanzio, J. C. 2011, in ASP Conf. Ser. 445, *Why Galaxies Care about AGB Stars II: Shining Examples and Common Inhabitants*, ed. F. Kerschbaum, T. Lebzelter, & R. F. Wing (San Francisco, CA: ASP), 29
- Stancliffe, R. J., Lugaro, M. A., Karakas, A. I., & Rijs, C. 2012, in AIP Conf. Proc. 1480, *First Stars IV from Hayashi to the Future*, ed. M. Umemura & K. Omukai (Melville, NY: AIP), 156
- Stephan, T., Trappitsch, R., Davis, A. M., et al. 2018, [GeCoA](#), **221**, 109
- Straniero, O., Domínguez, I., Cristallo, S., & Gallino, R. 2003, [PASA](#), **20**, 389
- Straniero, O., Gallino, R., Busso, M., et al. 1995, [ApJL](#), **440**, L85
- Takahashi, K., Boyd, R. N., Mathews, G. J., & Yokoi, K. 1987, [PhRvC](#), **36**, 1522
- Takahashi, K., & Yokoi, K. 1983, [NuPhA](#), **404**, 578
- Takahashi, K., & Yokoi, K. 1987, [ADNDT](#), **36**, 375
- Tomkin, J., & Lambert, D. L. 1983, [ApJ](#), **273**, 722
- Travaglio, C., Gallino, R., Amone, E., et al. 2004, [ApJ](#), **601**, 864
- Trippella, O., Busso, M., Maiorca, E., Käppeler, F., & Palmerini, S. 2014, [ApJ](#), **787**, 41
- Trippella, O., Busso, M., Palmerini, S., Maiorca, E., & Nucci, M. C. 2016, [ApJ](#), **818**, 125
- Tsuji, Y. 2009, [FIDyR](#), **41**, 064003
- Van Eck, S., Goriely, S., Jorissen, A., & Plez, B. 2001, [Natur](#), **412**, 793
- Van Eck, S., Goriely, S., Jorissen, A., & Plez, B. 2003, [A&A](#), **404**, 291
- van Winckel, H. 2003a, [ARA&A](#), **41**, 391
- van Winckel, H. 2003b, in IAU Symp. 209, *Planetary Nebulae: Their Evolution and Role in the Universe*, ed. S. Kwok, M. Dopita, & R. Sutherland (Cambridge: Cambridge Univ. Press), 91
- Ventura, P., Dell’Aglì, F., Lugaro, M., et al. 2020, [A&A](#), **641**, A103
- Vescovi, D., Cristallo, S., Busso, M., & Liu, N. 2020, [ApJL](#), **897**, L25
- Wood, P. R. 1990, in ASP Conf. Ser. 11, *Confrontation Between Stellar Pulsation and Evolution*, ed. C. Cacciari & G. Clementini (San Francisco, CA: ASP), 355
- Wood, P. R., & Sebo, K. M. 1996, [MNRAS](#), **282**, 958
- Zinner, E. 1998, [M&PS](#), **33**, 549